https://doi.org/10.5194/egusphere-2026-1377
Preprint. Discussion started: 12 June 2026

Late Glacial and Holocene landscape and permafrost evolution of the Barentsburg area, West Spitsbergen

Lutz Schirrmeister[1*], Nikita Demidov[2], Vasily Demidov[2], Paul Overduin[1], Walter Schirrmeister[3], Diana Soloveva[2], Sergey Verkulich[2], Sebastian Wetterich[1,4]

[1] Permafrost Research Section, Alfred Wegener Institute Helmholtz Center for Polar and Marine Research, Potsdam, Germany

[2] Arctic and Antarctic Research Institute, St. Petersburg, Russia

[3] independent researcher: Zechliner Str. 24, Berlin, Germany

[4] Current address: Institute of Geography, Technische Universität Dresden, Dresden, Germany

*Corresponding author: Lutz Schirrmeister, Lutz.Schirrmeister@awi.de

Abstract

The postglacial landscape evolution on West Spitsbergen provides insights into the interplay among glacial retreat and rebound, marine transgression, and permafrost aggradation, all of which are driven, or at least superimposed, by climate dynamics. To gain a new understanding of this interplay, a total of 19 permafrost drill cores, complemented by one natural exposure reaching depths of 5-25 m below the surface, were studied. The sampling heights span from 74 m above sea level to 4 m below sea level. The drill transect extends approximately 20 km inland from the marine terraces at Isfjorden (sub-area A), along the Grønfjorden (sub-area B), the Grøndalen (sub-area C), and the Hollendardalen (sub-area D) valleys in the wider Barentsburg area. Detailed cryolithological descriptions, hydrochemical and sedimentological analyses, and radiocarbon dating were employed to infer the spatial and temporal evolution of regional permafrost following deglaciation and sea-level adjustment.

The sediment composition is highly variable, ranging from clayey silt to gravelly sand (mean grain size: ca. 10-10,000 µm). Instead, the biogeochemical composition reveals relatively small differences in total organic carbon (TOC) and total nitrogen (TN) contents, as well as in stable carbon isotope ratios (δ13C) and in the TOC/TN ratio of organic matter. Likewise, the mass-specific magnetic susceptibility data exhibit relatively low variability. Ice and water extracts with low electrical conductivity, relatively low anion and cation concentrations, and a wide spread on the PIPER plot suggest a terrestrial origin of the ground ice. However, in some places, high conductivity and a dominant sodium-chloride composition indicate marine and/or cryopeg influence. Applicable radiocarbon dates are younger than 11 cal kyr BP. Older radiocarbon dates, starting from 37.8 cal kyr BP, are disputable and very likely contaminated by carbon from surrounding Tertiary coal deposits and, therefore, not considered in the present study.

Three major stages of Late Glacial and Holocene landscape evolution were identified: (1) deglaciation, (2) marine transgression, and (3) permafrost formation. The latter differentiates into three sub-stages characterized by (a) periglacial, fluvial, and alluvial deposition, (b) pingo formation, and (c) slope and alluvial deposition and pingo degradation.

As the High Arctic and thus the permafrost have recently experienced strong warming and substantial landscape changes, their evolution over geologic timescales warrants fundamental research to better understand climate-permafrost interactions. In this context, the present study provides insights into permafrost's response to Late Glacial and Holocene environmental changes.

Keywords: High Arctic, geochronology, sedimentology, ground ice hydrochemistry, pingo

https://doi.org/10.5194/egusphere-2026-1377
Preprint. Discussion started: 12 June 2026

1. Introduction

The High Arctic islands are important yet understudied sites for understanding current, past, and future climate, as well as Arctic environmental variability. The Spitsbergen Archipelago represents the first Arctic landmass along the path of western atmospheric transport and the warming influence of the Gulf Stream, making its permafrost particularly sensitive to atmospheric and oceanic changes. High-amplitude relative sea level change and glaciation-deglaciation processes during the late Quaternary also contributed to the instability of sediments and permafrost on Spitsbergen.

Geoscientific research on Spitsbergen has a long tradition, spanning approximately 150 years, with a primary focus on meteorology, geomorphology, geology, and glaciology. Permafrost studies focused on periglacial processes, temperature monitoring, and engineering (e.g., Liestøl, 1977; Humlum, 2003; Christiansen et al., 2003, 2010, 2019, 2021). Quaternary studies have been undertaken during the last decades (e.g., Landsvik et al., 1988, 1998; Mangerud et al., 1987, 1992; Mangerud and Svendsen, 2018; Svendsen et al., 1992, 1996), but past permafrost dynamics are rarely addressed. The late Pleistocene deglaciation of the Spitsbergen Archipelago and subsequent landscape development have been studied by, e.g., Farnsworth et al. (2020a, b) and Snyder et al. (1994, 2000), indicating that the glacial retreat coincided with Lateglacial-to-early Holocene climate warming across the entire archipelago. Temperatures during the last glaciation of Spitsbergen are assumed to have been considerably lower than today, while the climate during long periods of the Holocene has been significantly warmer than today, indicating likely permafrost degradation. The glacial history of the archipelago and the Barents Sea during the last glacial cycle is still debated. Contradicting models of a large ice sheet (Denton and Hughes, 1981) and of limited glaciation with ice-free areas along the western and northern coasts (Mangerud et al., 1987) have been proposed.

Simultaneously, with climate warming and deglaciation, a rebound of approximately 100 m occurred during the Holocene (Salvigsen, 1981). The oldest radiocarbon age of 12.740 ± 190 yr BP (14.425 ± 637 cal yr BP) is derived from marine mollusks (*Nucula tenuis*) in deposits of Linnévatnet Lake, approximately ten kilometers west of Barentsburg (Mangerud and Svendsen, 1990). Sharin et al. (2014) published radiocarbon dates from marine mollusk shells from the south bank of the Isfjord and the west bank of the Grønfjord, indicating middle and early Holocene ages of 11.7-6.6 cal kyr BP.

Landvik et al. (1988) discussed how glacial history and sea-level changes have controlled the distribution and thickness of permafrost in the region, although on-site investigations of past permafrost dynamics are rare. The presence of late Holocene permafrost near present-day sea level in central Spitsbergen is indicated by dating of both pingo and ice-wedge initiation (Svensson, 1971; Yoshikawa and Harada, 1995; Jeppesen, 2001). The presence of pre-Holocene and Holocene deposits in Adventdalen, and their division into epigenetic and syngenetic permafrost, was reported by Gilbert et al. (2018).

Since 2016, permafrost research has been resumed as part of the Russian Scientific Arctic Expedition on the Spitsbergen Archipelago (RAE-S) in Barentsburg, led by the Arctic and Antarctic Research Institute in St. Petersburg (Figure 1; Demidov et al., 2020a, 2020b). A permafrost monitoring network was established in this area (Demidov et al., 2016, 2025) in accordance with GTN-P (Global Terrestrial Network for Permafrost; Biskaborn et al., 2019) and RNS BPM (Russian National System of Background Permafrost Monitoring) standards (Demidov et al., 2025). Based on archive and own data, typical permafrost-hydrogeological conditions were identified, and cryogenic structures, the nature of salinization, and active-layer monitoring results were described in detail by Demidov et al. (2020a, 2020b). Further studies of internal pingo structures (Demidov et al., 2019, 2021), pingo distribution on Spitsbergen (Demidov et al., 2022), and local rapid permafrost thaw (Demidov et al., 2024) have been conducted.

The present study builds on ongoing research and aims to identify spatial and temporal changes in Late Glacial and Holocene permafrost conditions on West Spitsbergen in conjunction with deglaciation, climate change, and sea-level change. In particular, the following research topics were addressed:

- determination of the geological structure of Quaternary deposits in the Barentsburg region;
- radiocarbon age, and the environmental conditions of deposition;

https://doi.org/10.5194/egusphere-2026-1377
Preprint. Discussion started: 12 June 2026

- sediment freezing and the division of sediments into epigenetic and syngenetic permafrost;
- timing of deglaciation, sea regression, and pingo formation.

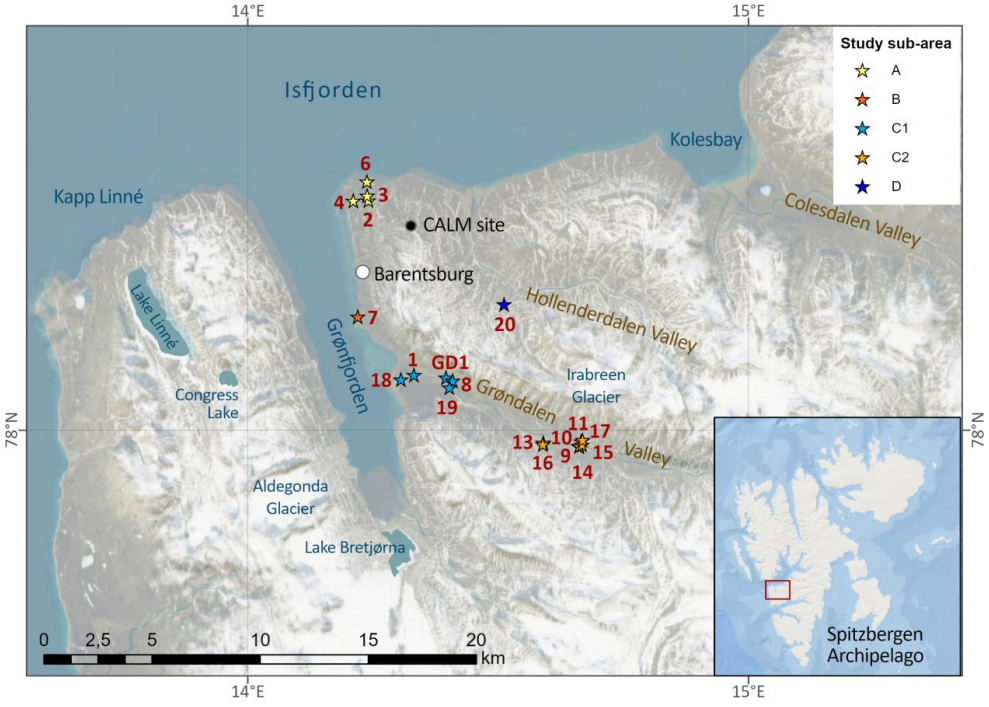

Figure 1 Position of the study area and the individual study sites in West Spitsbergen. The marked locations indicate drill cores and the profile GD-1 considered in the present study (Table 1). Map created by Sebastian Laboor, AWI Potsdam (Service Layer Credits: Source: Powered by Esri, Maxar, GeoEye, Earthstar Geographics, CNES/Airbus DS, USDA, USGS, AeroGRID, IGN, Garmin, GEBCO, NOAA NGDC, and the GIS User Community).

2. Study area

The study area is located in Nordenskiöld Land on the west coast of West Spitsbergen (Figure 1). The west coast, bordered by the Greenland Sea, is characterized by numerous narrow, deep fjords. To the west of the Grønfjord, mountain ranges formed by crumpled rocks with steep folds extend in a meridional direction. To the east of the Grønfjord, a deeply cut erosion network adds to the gently bedded rocks. The mountain peaks reach heights of 900 m above sea level (asl).

West of the Grønfjord, with relatively high submeridional ridges intercepting moisture from the Atlantic Ocean, large mountain ranges and intermittent glaciers are present. East of the Grønfjord, the mountain ranges are mostly glacier-free. Only in the upper reaches of the valleys are small hanging and mountain-valley glaciers present. During the last century, glaciers in western Nordenskiöld Land have undergone widespread shrinkage due to climate warming (Mavlyudov et al., 2012). From 1936 to 2017, glacier areas decreased by an average of 49.5% in total, and the outer edge receded by several kilometers (Chernov and Muravyov, 2018).

Geologically, the area lies at the junction of two large first-order structures (Krasilshchikov, 1973): the horst anticline on the western coast of Spitsbergen and the western Spitsbergen Graben. The junction zone of these two structures is the Western Fault Boundary Zone (Livshitsch, 1973). The structures of

https://doi.org/10.5194/egusphere-2026-1377
Preprint. Discussion started: 12 June 2026

the West Spitsbergen graben trough, located to the east and southeast of Grønfjord, consist of sedimentary rocks of Lower Cretaceous and Paleogene age, deposited in subhorizontal or gently sloping environments. These sediments are represented by alternating layers of sandstone, siltstone, and argillite. Among the Paleogene sediments, coal, bentonite clays, and lenses are also present. Cretaceous sediments appear to surface only in a small area in the coastal part of the Grønfjord and the Isfjord.

The geological structure of the western bank of the Grønfjord is more complex (Sirotkin et al., 2017). Here, ancient rocks representing the structures of the mountain anticline of the western coast of Spitsbergen come to the surface. The Precambrian rocks are metamorphosed and consist of micaceous chlorite shales, marble, quartzite, metabasite, and metatillite. In addition to siltstones, argillites, and sandstones, which are typical of the entire study area, Upper Paleozoic-Mesozoic sedimentary rocks include limestones, dolomites, gypsum, and phosphorites. All rocks are crumpled into systems of conjugate folds with drops on wings at angles of 20 - 90°, which are complicated by a series of faults, as well as dikes and sills of Mesozoic dolerites.

Quaternary sediments include colluvial, proluvial, eluvial-deluvial, alluvial, fluvioglacial, and glacial deposits, all of which are typical of mountainous regions. The Quaternary cover deposits, except for the seasonally unfrozen active layer and taliks in the ground, are completely frozen.

The landscape inventory comprises watershed peaks, valleys, glacial moraines, and coastal plains. On the summits, mountain slopes, and moraines, primary and desert arctic soils with highly sparse grassy-marsh-lichen groups are common. In valleys and on sea terraces, typical Arctic and arctic-tundra soils are common (Belousov et al., 1983).

According to Elvebakk (2005) the study area falls within the *Cassiope tetragona* tundra and the Mesic, acidic tundra characterized by *Luzula confusa*. *Salix polaris* predominates in the vegetation cover, and Poaceae and Cyperaceae also play an important role in the area. Further detailed descriptions of the vegetation in the study area have been published in Koroleva (2016) and Koroleva et al. (2008).

The climate of the area is significantly influenced by the warm West Spitsbergen Current, the northernmost branch of the Gulf Stream, as well as warm and humid air masses from the Atlantic Ocean. Therefore, the air temperature here is higher than one would expect in these High Latitudes. The polar day in Barentsburg lasts 125 days, and the polar night lasts 112 days (Obidin, 1958). According to Demidov et al. (2020b), the first Soviet weather station on the archipelago was established at the Grumant mine in 1932 and moved to Barentsburg in 1933 (WMO index 20107). Furthermore, the Green Harbour Norwegian Weather Station (WMO index 99821) was operated on Cape Finneset from 1911 to 1930. Data from these stations enable the assessment of centennial trends in air temperature variation. The mean annual air temperatures in the Barentsburg area changed from –10°C in 1912 to –2°C in 2018. According to data from the Barentsburg weather station, precipitation has also increased. The meteorological station in Barentsburg at 75 m asl recorded a mean annual air temperature of –2.8 °C and a mean annual precipitation of 583 mm from October 2016 to September 2022. Most of the annual precipitation occurs from October to March, when cyclonic activity is particularly active. Precipitation is lowest from April to July when stable anticyclonic weather prevails. In general, there is 1.5-2 times more precipitation in winter than in summer (Antsiferova et al., 2020).

The permafrost thickness in the Barentsburg area varies with morphology, ranging from 100 m near the seashore to 300-540 m in the mountain and upland areas. The permafrost thermal state and active-layer thickness, based on existing permafrost monitoring sites in Spitsbergen, maintained by national programs in Italy, Russia, Germany, Poland, and Norway, were most recently reported by Christiansen et al. (2021). Mean annual temperatures at the permafrost surface ranged between –0.5°C and –4.0°C, and permafrost temperatures, at or close to the depth of zero-annual amplitude, varied from –1.1 °C to –5.2 °C. The thickness of the active layer, measured in autumn 2017, ranged from 49 to 300 cm, with a general range of 100 to 200 cm.

https://doi.org/10.5194/egusphere-2026-1377
Preprint. Discussion started: 12 June 2026

The study area is divided into five sub-areas (Figure 1, Table 1) stretching from north to southwest including the marine terraces at the Isfjorden, north of Barentsburg (sub-area A), the fjord terrace at Kap Finneset, south of Barentsburg (sub-area B), and the Grøndalen Valley southwest of Barentsburg from the mouth to the Grønfjorden (sub-area C1) to the middle part of the valley (sub-area C2) (length approx. 10 km), and the Hollendardalen Valley (sub-area D), north of the Grøndalen Valley.

3. Materials and methods

3.1 Fieldwork

Permafrost drilling was undertaken during the summer season in 2016 and during the spring season in 2017, 2019, and 2020, and the outcrop GD 1 was sampled in summer 2015 (Table 1) within the framework of the RAE-S. The permafrost cores were obtained with a portable gasoline-powered rotary drilling rig (UKB 12/25, Vorovskiy Machine Factory, Ekaterinburg, Russia). The device uses no drilling fluid and relies on maintaining the core's frozen condition to ensure stratigraphic integrity and prevent downhole contamination of its sedimentological characteristics. Core diameters were 109 mm for the upper parts and 73 mm for the lower ones. The core pieces were lifted to the surface at intervals of 30-50 cm. Each segment was characterized by visible features, including grain size, color, organic content, sediment, and ice structures (French and Shur, 2010). After documentation and cryolithological description, the core pieces were sealed. The deposits were sampled from within intervals of about 0.5 to 1 m for further analysis. Samples were partially frozen for transport, whereas others were kept unfrozen.

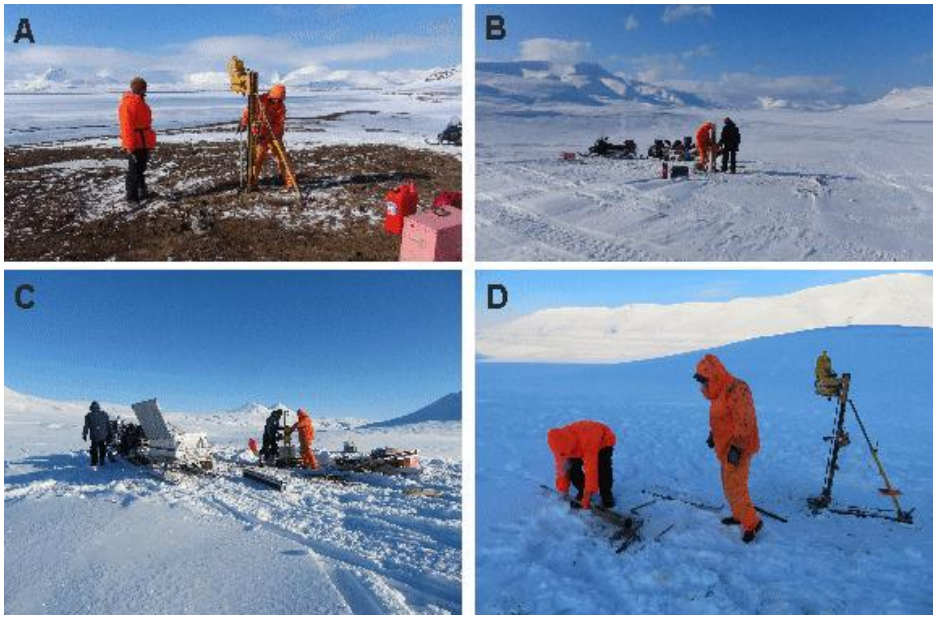

Figure 2 Pictures from the drilling procedures in the study area. A: drilling borehole Bbg 8, Grøndalen, April 2017; B: drilling borehole Bbg 9 (pingo Fili), Grøndalen, April 2018; C: drilling borehole Bbg 20, Hollendardalen, April 2020; D: drilling borehole Bbg 9 (pingo Fili), Grøndalen, April 2018.

https://doi.org/10.5194/egusphere-2026-1377
Preprint. Discussion started: 12 June 2026

Table 1 Study sites, study years, depth, altitudes, and the coordinates of the Barentsburg (Bbg) drill cores and the Grøndalen (GD) outcrop.

Sampling site	Year	Depth (m)	Altitude (m asl)	Coordinates	Sub-area
Bbg 2	2016/17	7.5	75	78.09504 °N, 14.24096 °E	
Bbg 3	2016/17	~ 4	60	78.09695 °N, 14.23810 °E	
Bbg 4	2016/17	~ 2	87	78.09493 °N, 14.21062 °E	A
Bbg 5	2016/17	~ 4	43	78.09856 °N, 14.23299 °E	
Bbg 6	2016/17	~ 2	9	78.10282 °N, 14.23794 °E	
Bbg 7	2016/17	12.6	8	78.04703 °N, 14.21962 °E	B
Bbg 1	2016	~ 2	2	78.02289 °N, 14.331806 °E	
GD 1	2015	3.7	16	78.02181 °N, 14.39566 °E	
Bbg 8	2016/17	21.25	18	78.02056 °N, 14.40907 °E	C1
Bbg 18	2020	5.0	1	78.02107 °N, 14.30550 °E	
Bbg 19	2020	6.0	9	78.01773 °N, 14.40249 °E	
Bbg 13 (pingo Nori)	2019	21.2	42.5	77.99483 °N, 14.59009 °E	
Bbg 16	2020	7.0	35	77.99416 °N, 14.58904 °E	
Bbg 9 (pingo Fili)	2016/17	25.0	49	77.99355 °N, 14.66211 °E	
Bbg 10 (pingo Fili)	2016/17	12.0	53	77.99332 °N, 14.66114 °E	C2
Bbg 11 (near pingo Kili)	2016/17	5.4	44	77.99531 °N, 14.66538 °E	
Bbg 14	2019	4.0	49	77.99354 °N, 14.66173 °E	
Bbg 15 (pingo Kili)	2019	13.8	60.5	77.99398 °N, 14.66742 °E	
Bbg 17	2020	3.5	43	77.99592 °N, 14.66862 °E	
Bbg 20	2020	12.0	68	78.05216 °N, 14.51170 °E	D

3.2 Laboratory work

Laboratory analyses have been carried out at the Barentsburg RAE-S station. Here, gravimetric moisture content (ice content) was measured by weighing samples before and after drying at 50 °C, and the weight loss was expressed as a weight percentage (wt%). Hydrochemical analyses were done from water extractions of sediment samples. For this, the material was dried and sieved through a 1 mm mesh. Approximately 20 g of the sediment was suspended in 100 mL of deionized water and filtered through a 0.45 µm nylon mesh within 3 minutes after stirring. Electrical conductivity (EC, measured in µS cm^{-1}) and pH values (accuracy ± 0.002) were determined using a Mettler Toledo Seven Compact S 220 device. EC values were converted to general ion content (accuracy ± 0.5%) and expressed in mg L^{-1}.

Major anions and cations in the water extracts were analyzed by ion chromatography (Shimadzu LC-20 Prominence) equipped with the Shimadzu CDD-10AVp conductometric detector and ion exchange columns for anions (Transgenomic ICSep AN2) and for cations (Shodex ICYS-50). Calibrations were performed in two sensitivity modes in the total range from 0.02 to 4 mg L–1 for Cl– and from 0.1 to 20 mg L–1 for SO42-, Na+, K+, Ca+, Mg+. The quantification limit was 0.02 mg L–1 for Cl– and 0.1 mg L–1 for SO42- and for cations, while precision errors were between 5% (for concentration range 0.1-4 mg L–1 Cl-, 5-20 mg L–1 SO42-, 2-20 mg L–1 Na+, K+, Ca+, Mg+) to 15% (for concentration range 0.02-0.1 mg L–1 Cl-, 0.1-5 mg L–1 SO42-, 2-20 mg L–1 for Na+, K+, Ca+, Mg+).

The bicarbonate concentration was calculated directly from inorganic carbon content measured by a Shimadzu TOC-L analyzer. Samples were treated with HCl, sparged, and analyzed by infrared detection in a TOC-L infrared gas analyzer (NDIR) with a detection limit of 4 µg L–1. The contribution of carbonates and dissolved CO2 to the inorganic carbon content was considered negligible based on pH measurements. The quantification limit for inorganic carbon was 0.1 mg L–1, and the precision

https://doi.org/10.5194/egusphere-2026-1377
Preprint. Discussion started: 12 June 2026

error did not exceed ±6%. Clean ice samples were analyzed directly using the aforementioned equipment in Barentsburg.

The geochronology was established based on 49 Accelerator Mass Spectrometry (AMS) radiocarbon dates using the Mini Carbon Dating System (MICADAS) facility at the Alfred Wegener Institute Helmholtz Center for Polar and Marine Research (AWI). Details of laboratory procedures and sample pretreatment are provided in Mollenhauer et al. (2021). The dated material was obtained by hand-picking terrestrial plant remains from freeze-dried samples and from decarbonated bulk samples, as well as from several bulk samples based on $\delta^{13}C$ measurements. The preparation for AMS dating included TOC analyses (seven samples using a CHNS analyzer) and graphitization (two samples using the AGE 3 system, Ion Plus, Switzerland). Remaining samples were prepared accordingly at the Center for Applied Isotope Studies of the University of Georgia (USA), where the AMS radiocarbon ages were also measured using the 1.5SDH Pelletron AMS (Zazovskaya et al., 2016). All radiocarbon dates were calibrated using the IntCal20 calibration dataset (Reimer et al., 2020). Ages are given as calibrated years before present (cal yr BP).

At the AWI Potsdam Sedimentological Laboratory, sediments were freeze-dried (Zirbus Subliminator 3-4-5), manually homogenized, and split into sub-samples for further analyses. Grain-size distribution (GSD) analyses were carried out using a combination of wet-sieving (Vibratory Sieve Shaker ANALYSETTE 3, Fritsch) and laser diffraction particle size analyzer (Malvern Mastersizer 3000) after removing organic matter with hydrogen peroxide (3%). Sieving fractions were < 1, 1-2, 2-5, 5-6.3, 6.3-10, and > 10 mm. The laser diffraction analyses were carried out over the range of 0.1 µm to 1 mm, after sieving to <1 mm. The grain-size classification was based on Reineck and Sing (1980) and Wenthworth (1922). Grain-size data were evaluated using the Gradistat v9 software (Blott and Pye, 2001).

Mass-specific magnetic susceptibility (MS), which indicates the content of magnetic and magnetizable minerals, was measured after the sample was dried, homogenized, and split using a Bartington MS2 instrument equipped with the MS2B sensor. The data are expressed in SI units ($10^{-8}m^3kg^{-1}$). The low-frequency (LF) data are presented.

The total elemental carbon (TC) and nitrogen (TN) contents were measured with a VARIO-EL-III Element Analyzer, while total organic carbon (TOC) content was measured with the VARIO MAX C. These data were expressed in weight percentage (wt%) and further used to characterize basic organic matter (OM) quantity and quality parameters. Using the TOC and TN values, the TOC/TN ratio was calculated to determine the degree of OM decomposition, as described by Carter and Gregorich (2007). Total inorganic carbon (TIC) was calculated as the difference between TC and TOC. For TOC and $\delta^{13}C$ analyses, samples were decalcified for 3 h at 95°C by adding 1.3 N HCl. The $\delta^{13}C$ of TOC was measured with a Finnigan DELTA S mass spectrometer equipped with a FLASH elemental analyzer EA 2000 and a CONFLO IV gas mixing system. The $\delta^{13}C$ values are expressed in delta per mil (δ‰) notation relative to the Vienna Pee Dee Belemnite (VPDB) standard with an uncertainty of 0.15‰. Variations in $\delta^{13}C$ indicate changes in local vegetation and the degree of OM decomposition (Hoefs, 1997).

Pollen extraction from sediments was performed in accordance with Grischuk's separation method (Grichuk and Zaklinskaya, 1948) with using heavy liquid. In addition, 7-mm ultrasonic fine-sieving during 4 min was used for all samples (Cwynar et al.,1979). Pollen and spore identification was carried out using published sources (Kupriyanova and Alyoshina, 1972, 1978; Moore et al., 1991; Savelieva et al., 2013) and reference collections at the Saint-Petersburg State University. The minimum amounts of pollen grains were counted in the interval from 370 m to 120 cm and other cases from 50 to 250 pollen grains. Tilia/Tilia-Graph/TGView software (Grimm, 1993, 2004) was used for calculating pollen percentages and for plotting the pollen diagram.

Diatom analysis of 14 samples collected from each sediment stratum was performed at the Arctic and Antarctic Research Institute (AARI) laboratory, St. Petersburg. Diatom analysis was carried out using a

https://doi.org/10.5194/egusphere-2026-1377
Preprint. Discussion started: 12 June 2026

standard method (Diatoms ..., 1974) using an aqueous solution of sodium pyrophosphate ($Na_4P_2O_7 \cdot 10H_2O$) and a heavy liquid with a density of 2.29 g/cm³. A medium with a refractive index of 1.67–1.68 was used to prepare permanent slides. Species identification of diatoms was performed using a MICMED-5 light microscope equipped with a digital camera based on data from atlases and monographs (Krammer & Lange-Bertalot, 1986, 1988, 1991; Chudaev & Gololobova, 2016; Kulikovskiy et al., 2017, among others). The percentage abundance of each taxon was determined by counting 300 valves per sample. The PanPlot software was used to construct diagrams. (Soloveva et al. (2026).
Core descriptions and analytical data are available in the PANGAEA database (Schirrmeister et al., 2023).

4 Results

4.1 Sub-area A (Isfjord terraces)

Sub-area A is situated north of Barentsburg on the up to 100 m asl high Holocene marine terraces (Figure 1), which overlay Cretaceous and Paleogene fractured sandstones and slates (Demidov et al., 2016). The terraces correspond to different Holocene sea levels during the postglacial (rebound) rise of Spitsbergen, when sea level remained relatively constant for a longer period.
Permafrost features, such as solifluction structures, frost boils, and frost cracks, are observed on the Holocene marine terraces. In contrast, thermokarst and thermo-erosional traces are only visible in disturbed areas where drilling rigs were installed during the 1930s-1950s geological exploration.
The cores Bbg 2 to 6 were drilled at different terrace levels between 10 and 87 m asl (Table 1, Table S 1.1). The thickness of accumulated deposits varies from 2 to 7 m. The permafrost table was located at depths of 1.5-2 m (Figure 3). The marine terrace deposits exhibit similar cryolithology. From the top, there are clay and sand deposits approximately 1.5 m thick, followed by gravels and pebbles within dark, sandy-silty aggregates. The cryostructures are massive in sandy, gravelly, and pebble layers, while frozen clays exhibit reticulate and layered cryostructures, including ice-rich ground and ice layers up to 20 cm in thickness (Table S1.1).
The highest absolute ice (moisture) content, reaching up to 57wt%, was measured in core Bbg 3 at a depth of 2.5 m. The lowest value, 1.3 wt%, was from Bbg 2 at a depth of 3.6 m. In most cases, the absolute ice content ranges from 10 to 30wt%. The 7 m long core Bbg 2 was studied in detail sedimentologically. The MS range between 8 and 16 $10^{-8} m^3 kg^{-1}$ (Figure 3). The TOC contents vary between 0.8 and 1.2wt%, and the $\delta^{13}C$ values between –26.03 and –25.38 ‰. The sediment consists dominantly of silt with some coarser sandy layers. The mean grain size ranges from 18 to 84 µm in the middle part of the core, with a sandy horizon at approximately 5 m depth (163-305 µm). The lowermost sample (at 7 m depth) and the uppermost samples (at 2.3-1.85 m depth) are coarser, with mean grain diameters of 355 µm and 635 µm, respectively.
Hydrochemical analyses of water extracts from core samples were performed on all five cores of sub-area A. The pH values range from very weakly acidic (6.2) to very weakly basic (8.4). EC values in core Bbg 2 range from 682 to 1308 µS cm^{-1} between 2.7 and 7 m depth to much lower values of 18-195 µS cm^{-1} in the upper part of the core above 2.7 m depth. In the cores Bbg 3 and Bbg 5, the deeper sections (3.3-3.8 m) show slightly higher EC values. The upper two meters of the cores Bbg 2, 3, 4, and 6 are dominated by potassium and chloride. In the deeper sections of these cores, the hydrochemical composition changes to higher sodium and sulfate contents (Figure 3). In core Bbg 5, Na^+ (30-60%) and K^+ (31-59%) cations dominate the ionic composition, while the anions, HCO_3^-, SO_4^{2-}, and Cl^- occur in similar proportions.

https://doi.org/10.5194/egusphere-2026-1377
Preprint. Discussion started: 12 June 2026

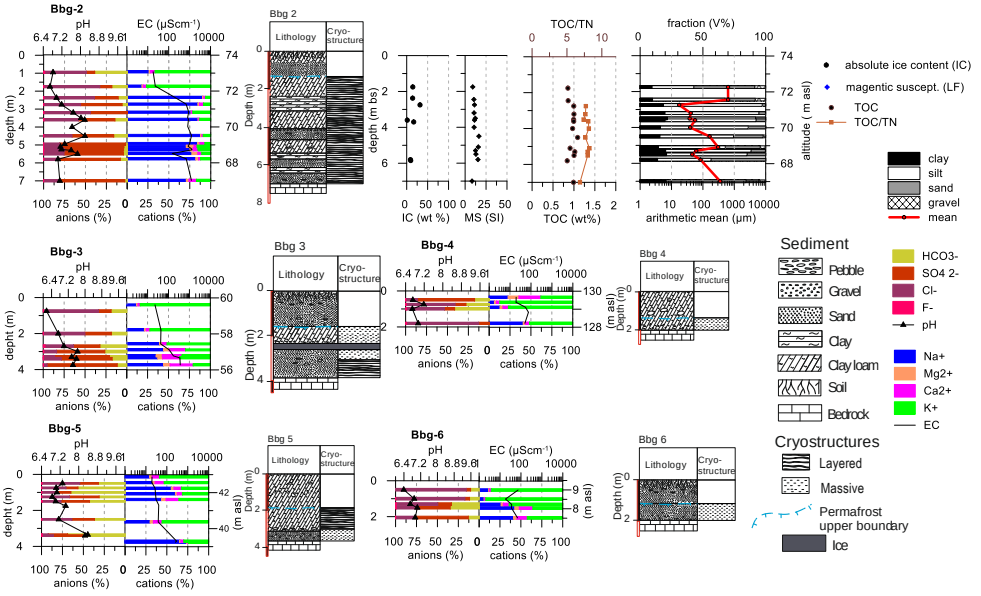

Figure 3 Cryolithological profiles, hydrochemical and sedimentological data from the sub-area A (Isfjord terraces).

4.2. Sub-area B (Kap Finneset)

Sub-area B is located at Kap Finneset, south of Barentsburg (Figure 1). Here, the core Bbg 7 was drilled on the beach of the Grønfjord at 8 m asl (Table 1, Table S1.2, Figure S3.2).

The borehole Bbg 7 reached the rock basement at 12.6 m depth (Figure 4). Above there were up to 12 m of loamy deposits, including a lot of wood remains and pebbles, topped by 0.3 m of ice. From 10.6 to 11.7 m, black clay, gray, and yellowish interbedded loam and sandy loam were obtained. The cryostructure is represented by ice lenses up to 0.4 cm thick, with a sub-horizontal orientation, and individual ice lenses up to 10 cm thick. From 8.5 to 10.6 m depth, gravel and crushed debris interlayered with dark sandy loam with plant remains were present, and an organic smell was noted. The cryostructure was predominantly massive, but ice lenses were found in the lower part, which contained marine mollusk shell fragments up to 3 cm long. Between 1.8 and 8.5 m in depth, the core was characterized by dark gray sand and gravel soil, sometimes containing silty aggregates and large pebbles. Some interlayers were cross-bedded, and separate interlayers consisted of clean sand. The cryostructure was continuously massive. The uppermost horizon from 0 to 1.8 m is built of gray sand with interlayers of gravel and pebbles. The permafrost table was observed at a depth of 1.8 m.

Ice content data are available at depths of 8.9 and 10.2 m (17.5 and 22.0 wt%). The MS is between 8.4 and 12.7 $10^{-8}m^3kg^{-1}$ (Figure 4). TOC is about 0.9wt% and the $\delta^{13}C$ values between –25.10 and –24.63 ‰. TN was below the detection limit; therefore, the TOC/TN ratio was not calculated. The sediment consists mainly of sand (25-51wt%) and silt (30-52wt%) with some gravel and clay (both 6-13wt%). The arithmetic grain-size mean varies between 500 and 938 µm.

The pH range is 8.4-8.2 in the clayey lower part, at depths of 10.8-12.4 m. The upper part is characterized by lower values between 6.8 and 7.8 (Figure 4). EC values are also higher (431-829 µS cm^{-1}) in the lower part and lower (16-279 µS cm^{-1}) in the upper part of the core. In the top four meters, Na^+(42-50%) and K^+ (31-46%) dominate. HCO_3^- (40-62%) dominates in this section, followed by SO_4^{2-}

https://doi.org/10.5194/egusphere-2026-1377
Preprint. Discussion started: 12 June 2026

(20-26%) and Cl^- (15-32%). At around 8 m depth, the composition of water extract is dominated by K^+ (73%) and Cl^- (58%).

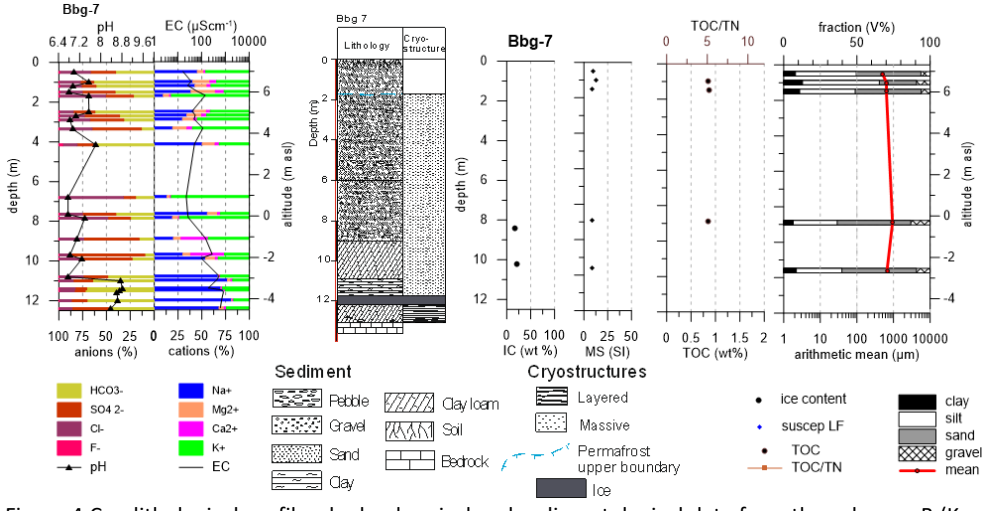

Figure 4 Cryolithological profiles, hydrochemical and sedimentological data from the sub-area B (Kap Finneset).

4.3. Sub-area C1 (lower reaches of the Grøndalen Valley)

In the lower reaches of the Grøndalen Valley, the boreholes Bbg 1, Bbg 8, Bbg 18, Bbg 19, and the outcrop GD 1 were studied (Figure 1, Table 1, Table S1.3).

The deepest reaching (21.5 m) and most detailed studied core Bbg 8 in sub-area C1 was drilled in 2016/17 on the northern site of the Grøn River about 3 km east of the river mouth (Figure S3.3). The larger part (5.05-21.5 m) consists of alternating pure ground ice and ice-rich, dark-gray, salty clay, with some thin, black, 1-2 mm-thick lenses and interlayers (Table S1.3). The cryostructure is reticulate, lens-like, layered, laminated, and partly porphyritic. Above at 1.5-5.05 m depth, the sediment consists of grayish to brown loam with some interlayers of silty sand (aleurit) and peat. The cryostructure is massive or reticulate layered. The uppermost part (0-1.5 m) is composed of gravel, coarse sand, or gray-brownish loam. The cryostructure is massive, porphyric, or horizontally layered lens-like (Figure 5).

The absolute ice content of Bbg 8 was 42wt% at the lowermost site (20.2 m), decreased to about 23-31wt% between 18.5 and 15.8 m depth, increased to 56wt% at 15.5 m, and changed several times further up (until 7.8 m depth) between 26 and 47wt%. The uppermost part of the core showed decreasing ice content, ranging from 10 to 35wt%. The MS values are relatively close to each other (11-17 x 10^{-8} m^3 kg^{-1}). Only at depths between 9.1 and 10 m, there are higher values (20.5 and 32.6 × 10^{-8} m^3 kg^{-1}). The TOC content ranges from 0.8 to 1.2wt%, the TOC/TN ratio from 5.6 to 11.2, and the δ13C values from –26.43 to –26.17 ‰. Silt is the main fraction (65-84wt%). Only in the upper meter, there is higher sand content of about 20 to 30wt% (Figure 5). Therefore, the arithmetic grain-size mean is mostly between 10.6 and 75.5 µm, and only in the uppermost core meter, thin sand layers (150-220 µm) occur.

The pH values range between 5.4 and 8.4. Whereby the weakly basic values are concentrated in the upper meter of the core. Only between depths of 5.8 and 5.7 m does the pH again become more basic, reaching 8.2. The EC values in the upper meter are very low (27-215 µS cm^{-1}), but then rise rapidly to values between 1,267 and 12,100 µS cm^{-1}. Further down, the EC values fluctuate between 347 and

https://doi.org/10.5194/egusphere-2026-1377
Preprint. Discussion started: 12 June 2026

5,530 µS cm–1 (Figure 5). K^+ levels are relatively high in the upper meter (16-77%), but then drop quickly to 1-9.5%. The rest of the core is Na^+-dominated (84-99%). For the anions, there are relatively high HCO_3^- values (21-25%) between 0.3 and 0.7 m, with lower Cl^- (26-60%) and SO_4^{2-} (14-30%) values. For most of the core, Cl^- values range from 66 ± 18% on average, and SO42– values range from 29 ± 21% (Figure 5).

The outcrop GD 1 (Verkulich et al., 2018; Soloveva et al., 2026) was studied on the slope of a terrace near the core site of Bbg 8. The 3.7 m thick profile (Figure 5, Table S1.3) contains bluish-gray, diagonally layered sandy silt with inclusions of plant remains and gravel, and ice lenses in the lowermost part (3.15-3.7 m). This horizon was followed by sub-horizontal layered pebbly gravel with lenses of silt with gravels and pebbles (1.55-3.15 m depth). Above, between 0.35 and 1.55 m depth, interbedded bluish-gray silt and fine sand with inclusion of plant material and peaty interbeds occur. Finally, brown silt and sand with a large amount of gravel and pebble inclusions were found between 0.07 and 0.35 m in depth. The profile was topped by a 7 cm-thick peated litter.

The short core Bbg 1 was drilled near the mouth of the Grøn River and consists of about 2 m of pebbly sand above bedrock. The permafrost table was found at a depth of about 1 m. The cryostructures of the frozen ground below were layered (Figure 5).

The core Bbg 18 was drilled at the mouth of the Grøn River, and the core Bbg 19 was drilled in the riverbed of the Grøn River. These cores contain thawed, greyish silt in their lower parts (at depths of 4.0-5.0 m and 5.5-6.0 m, respectively). Above in Bbg 19 at 3.9 - 5.0 m depth, there was fine-grained sand with plant remains, rare horizontal gravel and loam layers, and strongly salty porewater. In core Bbg 18, the main part between 1.7 and 4.0 m depth consists of black freshwater silt with rare coarse pebbles, gravel, and sand. The cryostructure was massive, nesting or layered. Further up, gravelly sand, subhorizontally oriented, occurs up to the end of the cores, with a porous or massive cryostructure (Figure 5).

The absolute ice content of Bbg 18 and 19 was not analyzed. The MS values range from 9 to 14 × 10^{-8} m^3 kg^{-1} in Bbg 18. The TOC content between 1.1 and 1.8 wt% is slightly higher than in Bbg 8. The TOC/TN ratio ranges from 9.1 to 13.2, and the δ13C values range from –25.54 to –24.33 ‰. Although the silt content in Bbg 18 reaches 50 to 62wt%, the arithmetic grain-size mean is 776 to 1798 µm. This is due to the relatively high sand (9-27wt%) and gravel content (7-17wt%). The clay content ranges from 9 to 16wt%. Bbg 19 has higher MS values (15-20 x 10^{-8} m^3 kg^{-1}) in the lowermost section of the core (6.1-5.8 m). In the upper part of the core, the MS values range from 6.4 to 9.3 x 10^{-8} m^3 kg^{-1}. TOC contents are still slightly higher than in Bbg 18 (1.0-2.0wt%), and TOC/TN ratios range from 6.4 to 12.2. The $\delta^{13}C$ values range from –26.34 to –25.97 ‰. The grain size composition varies much more than in core Bbg 18. There are silty fine sand horizons with an arithmetic grain-size mean of 27 to 88 µm. Other horizons are much coarser, with grain-size means of 210 to 321 µm, 1028 µm, and 4870 µm at depths of 4.3 to 2.0 m, 5 m, and 0.5 m, respectively.

The pH values ranged from 7.9 to 9.3 for Bbg-18 and from 7.2 to 81 for Bbg-19. EC values vary between 984 and 1747 µS cm^{-1} in Bbg-18 and between 106 (0.5-0.6 m depth) and 3900 µS cm^{-1} (6-6.2 m depth) for Bbg-19. Cation shares are 40-89% for Na^+, 8-50% for K+, 2-26% for Ca2+, and 1-15% for Mg^{2+} in Bbg-18. Except for one sample at 0.5-0.6 m, core Bbg 19 is Na+-dominated (93-99%). The anion data of core Bbg 18 shows a division into two. The upper part (1.8-3.5 m depth) is SO_4^{2-} dominated (76-85%) while in the lower part (3.8-5 m depth) Cl^- (29-38%), SO_4^{2-} (41-48%), and HCO_3^- (15-28%) are about the same. In core Bbg 19, the Cl^- anion (72-90%) dominate in the lower part (2.0-6.2 m depth), while the upper part (0.5-1.7 m depth) contains SO_4^{2-} (27-50%), HCO_3^- (15-44%), and Cl^- (5-57%) at comparable shares.

https://doi.org/10.5194/egusphere-2026-1377
Preprint. Discussion started: 12 June 2026

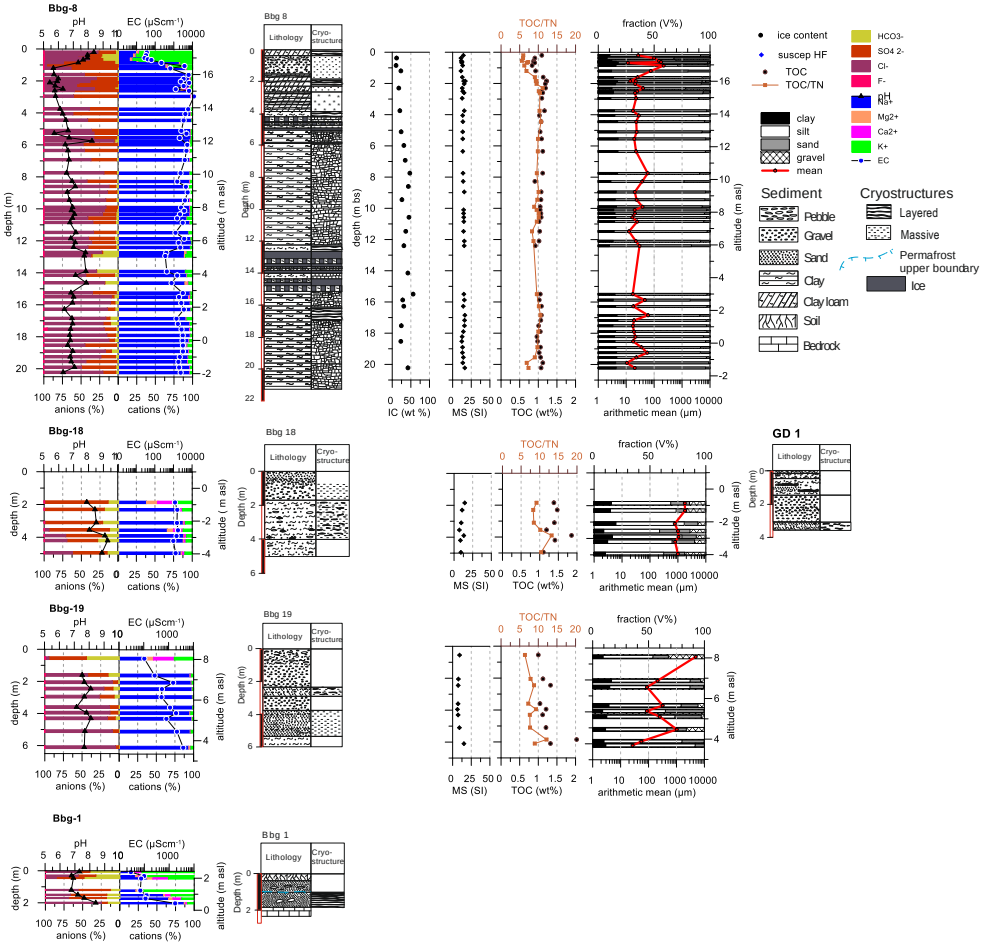

Figure 5 Cryolithological profiles, hydrochemical and sedimentological data from the sub-area C1 (lower part of the Grøndalen Valley.

4.4. Sub-area C2 (middle part of the Grøndalen Valley)

In the middle part of the Grøndalen Valley, within sub-area C2, several pingos were studied (Demidov et al., 2019, 2021, 2022; Figure 1, Table 1). Sub-area C2 is subdivided into C2 (A) and C2 (B) based on the differing prevalence and characteristics of the pingos.

4.4.1 Sub-area C2 (A)

The sub-area C2 (A) was investigated in the front part of the middle section of Grøndalen Valley. Here, the pingo Nori was drilled twice at about 5 km ESE from the core site Bbg 19 (Figure 1), resulting in core Bbg 13 on top of the pingo (20.5 m long) and core Bbg 16 (7 m long) at its southern edge (Demidov et al., 2021; Figure S3.4). In the lowermost part of core Bbg 13 (20.5-21.8 m depth), a gravel-pebble layer with up to 30% of loam and with a porous cryostructure was found. Between 18 and 20.5 m depth, transparent massive ice without bubbles, but with salty clay inclusions in places, was obtained, covered by subvertical, oriented gravel (17-18 m depth) with dark gray pebbles and coarse sand, and

https://doi.org/10.5194/egusphere-2026-1377
Preprint. Discussion started: 12 June 2026

dark gray loam, which tasted salty. Between 4.4 and 17 m depth, massive ice was found partly without bubbles, partly with organic matter inclusions, and some clayish inclusions (Figure 6, Table S1.4). Further up, gravel horizons with sparse pebbles and a massive or porous cryostructure were obtained. The core Bbg 16 was drilled about 75 m south at the edge of pingo Nori. The core consists mainly of medium-sized pebbles and gravel with clayey parts, and in the upper section, between 0.05 and 1.4 m in depth, there is clay. The cryostructure in the gravel horizons is porous and micro-lenticular in the upper, clayish part.

The absolute ice content of Bbg 13 (pingo Nori) ranged from 8 to 62wt% (Figure 6). Whereas the high contents in core Bbg 13 were at the top of the pingo above (3.5 m depth) and below (17.0-17.8 m depth) the ice core, at the edge of the pingo (Bbg 16), similar contents were measured at 3-4 m depth. In the lowermost sections of core Bbg 16, the ice content decreases to 10-25wt%. The MS values range from 8 to 11 $10^{-8}m^3kg^{-1}$ in these two cores. TOC values in core Bbg 13 at the top of the pingo range well below 1wt% between 0.6 and 0.9wt%). Higher values are found in core Bbg 16, varying from 0.8 to 2.4wt% (Figure 6). The TOC/TN ratio is 6.5 to 8.5 in core Bbg 13, and somewhat higher between 6.7 and 14.6 in core Bbg 16. The $\delta^{13}C$ values are again in a relatively small range between –26.41 ‰ and –25.84 ‰. The mean arithmetic grain size of the pingo Nori sediments (Bbg-13) ranges from 13 to 91 µm. Its grain-size distribution is dominated by 70 to 78wt% silt, while clay (13-19wt%) and sand (3-16wt%) are less present. At the edge of the pingo in core Bbg 16, the sediment is partly much coarser (23 to 5004 µm) and alternates more frequently between silty (up to 85wt%) and gravelly (up to 40wt%) horizons (Figure 6).

The pH values in the pingo Nori ice (Bbg 13) range from 9.6 to 7.0. Within the sediment layers below, in, and above the pingo ice core, the values range from 8.8 to 6.4 (Figure 6). EC values are relatively high in the lower section (sediment and pingo ice) of the core (21.8-14.0 m depth), ranging from 1616 to 5300 µS cm^{-1}. Further up (13.7-4.6 m depth), within the pingo ice, the values drop from 931 to 122 µS cm^{-1}. In the upper section (3.3- 0.0 m depth) in the sediment core, EC values drop further from 724 to 24.1 µS cm^{-1}. The lower section (below 18.0 m depth) of the core Bbg 13 (sediment and ice) is Cl^- dominated (80-99%). Then follows a sediment layer in which higher concentrations of SO_4^{2-} (2-37%) and HCO_3^- (14-55%) were measured. After that, the pingo ice is again Cl^- dominated (95-98%) from 16.7 to 14.0 m. From 13.7 m depth, a higher HCO_3^- content (8-37%) was measured. In the uppermost sediment core section from 3.4 m to the top, the Cl^- content decreases from 86% to 6% and the SO_4^{2-} (up to 19%), HCO_3^- (up to 71%) and the F^- (up to 8%) contents increase (Figure 6). Na^+ largely dominates the cation contents over almost the entire core (81-99%). Only in the uppermost meter are the Na^+ contents lower (34-61%). Ca^{2+} content is often less than 1%. However, several sections show higher Ca^{2+} values, both in the pingo ice (up to 12%) and in the upper sediment section (up to 15%). K^+ contents in the pingo ice are slightly higher between 9.1 and 6.4 m depth (2-11%) and then in the upper 1.5 m of the core (8-47%).

The core Bbg 16 from the pingo Nori edge has clearly lower pH values (4.9-7.2) and very low EC values (21-95 µS cm^{-1}). The cation contents were measured with a relatively similar mix of Na^+ (32-71%), K^+ (3-37%), and Ca^{2+} (7-38%). Mg^{2+} (2-17%) is less represented (Figure 6). The anion values are relatively well distributed between Cl^- (6-43%), SO_4^{2-} (35-72%), and HCO_3^- (11-48%).

https://doi.org/10.5194/egusphere-2026-1377
Preprint. Discussion started: 12 June 2026

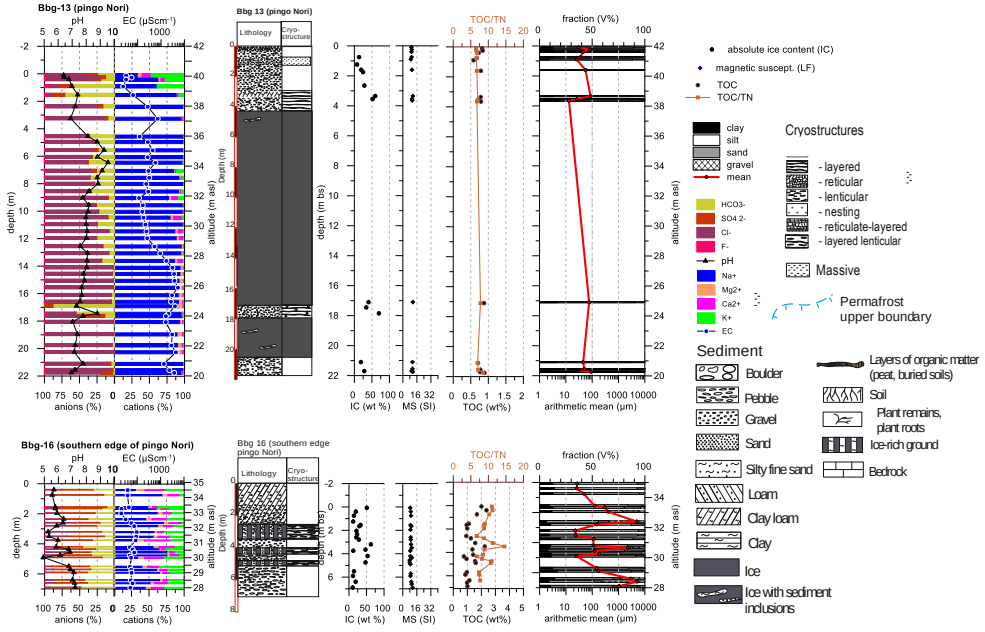

Figure 6 Cryolithological profiles, hydrochemical and sedimentological data from the sub-area C2 (A) (middle part of the Grøndalen Valley).

4.4.2 Sub-area C2 (B)

In the second pingo area in sub-area C2 (B) (Figure 1), boreholes were drilled into the pingo Fili (Bbg 9, 10, and 14) and pingo Kili (Bbg-15). One more core was drilled north of the pingo Kili (Bbg-11) and one in the Grøn River riverbed between the pingos Kili and Oin (Bbg-17, Figure S3.5). At the pingo Fili (1.8 km east of pingo Nori), the 25 m long core Bbg 9 was drilled at the top (Demidov et al., 2019). The lowermost part of core Bbg 9 (25.0-22.1 m) consists of ice-rich dark-gray clay with two transparent ice layers of 0.1 to 0.7 m thickness. From a depth of 23.5 to 15.5 m, the pingo ice core was drilled through almost transparent ice with sediment inclusions (1-2 cm) and numerous rounded air bubbles (1-5 mm). Further up (13.5 to 1.15 m depth), the ice was partly dirty with numerous sediment inclusions (Figure 7, Table S1.4). The uppermost part of the core was composed of brownish-gray loam with some gravel and small pebbles. The cryostructure was micro-lens-like, with an ice content of 10-15wt%. Core Bbg 14 comprises the upper section of the pingo Fili sediments. Between 4.0 and 1.35 m depth, clear pingo ice without bubbles but with occasional 1-2 mm inclusions of loamy material existed (Figure 7, Table S1.4). Further up, the core consists of medium brown loam with sparse gravel and small peat inclusions. The cryostructure consists of vertically oriented 1-2 mm wide streaks.

At the southern slope of the pingo Fili, the 12 m long core Bbg 10 was drilled. Between 12.0 and 6.2 m in depth, the sediment is composed almost entirely of ice-rich clay, with some gravelly grains and silt inclusions. Two ice layers, ranging in thickness from 0.05 to 0.2 m, occurred. The cryostructures were diagonally oriented reticulated lenses. The ice content has not been analyzed. At 6.2 to 5.9 m depth, a pebble horizon in a sandy matrix was found that was followed by 0.4 m of ice-rich ground. From 4.7 to 2.5 m depth, ice-rich clay that contains some small gravels. The cryostructure consists of reticulated lenses. The horizon at 2.5-0.4 m depth consists of sand or sandy loam with medium rounded gravels

https://doi.org/10.5194/egusphere-2026-1377
Preprint. Discussion started: 12 June 2026

and single small pebbles. The uppermost part (0.4-0.0 m depth was composed of a brownish sandy loam (soil) with single gravel grains and numerous plant residues (Figure 7, Table S1.4).

Between the pingo Kili and the about 500 m to the west located pingo Oin the core Bbg 17 was drilled. This core consists in the lower part (3.5-2.7 m depth) of interstratified silty sand with small gravel horizons and a porous and lens-like cryostructure horizon (Figure 7, Table S1.4). The upper part of the core (2.7-0.0 m depth) consists of gravel and pebbles with a loamy matrix.

The 13.8 m long core Bbg-15 (pingo Kili, Figure 7) consists in the lowermost part (13.3-13.8 m depth) of transparent ice without bubbles but with rare clayish inclusion. That ice is followed by fine-layered, slightly inclined silty clay (10.3-13.3 m depth). The cryostructure is lenticular, with coarse vertical lenses 2 cm long. At 10.1-10.3 m depth, a 20 cm thick sand with gravel is overlain by weakly inclined and interbedded silty loam (6.8-10.1 m depth) with lenses of black organic matter. The cryostructure is almost massive with single small lenses. From 6.6 to 4.2 m depth, several horizons of gravel with single pebbles alternate with horizontally stratified yellowish gray to dark gray sand horizons (Table S1.4). The uppermost part of the core, between 4.2 and 0.0 m depth, consists of gravel with pebbles and boulders, and some infill of unsorted sand.

About 150 m north of pingo Kili in the Grøn River floodplain, the 5.4 m long core Bbg 11 was drilled, which is formed by sandy loam with different parts of gravel and pebbles. Single horizons with more pebbles were found. The cryostructure was mostly massive.

The absolute ice contents of frozen deposits in sub-area C2 (B) are in a relatively low and narrow range between 4 and 27wt% in all studied cores (Figure 7). The MS values are between 10 and 15 x 10^{-8} m^3 kg^{-1}. Only one sample in core Bbg-9 at 22.45 m depth has a higher value of 29 $10^{-8}m^3kg^{-1}$. TOC values for most sections of the cores range from about 0.7 to 1.1wt%. Only in the uppermost sections up to approx. At a depth of 0.4 m, TOC content is higher, ranging from 1.5 to 8.8wt%. The TOC/TN ratio could not be determined for core Bbg-15 (Pingo Kili) because the TN content was below the detection limit of 0.1 wt%. The $\delta^{13}C$ values changed between -26.81 and – 26.10 ‰, except for the top 0.4 m in core Bbg 10 (–27.11 to –25.92 ‰). The arithmetic mean grain-size ranges from 29 to 147 µm, with a silt fraction of 63 to 81wt%, in the lower section of core Bbg-9 (pingo Fili). The uppermost part is still finer (18-24 µm). The grain-size composition of the sediments on the slope of this pingo (Bbg-10) varies much more, with mean grain size values between 18 and 9784 µm. The lower section of the core (12.0-8.0 m depth) is dominantly silty (silt 71-79wt%). In the middle section (8.0-3.4 m depth), silty (79-83wt%) and gravelly (21-79wt%) horizons alternate. The uppermost section (3.4-0.0 m depth) is dominated by gravel (24-78wt%). The core Bbg-15 of pingo Kili is silty (63-80wt%) with a grain-size mean of 17 to 112 µm (Figure 6). The core Bbg-11 north of pingo Kili has a coarser composition with a grain-size mean of 340 to 1131 µm. Only the uppermost 0.2 m are finer (52-69 µm). Between the two pingos, Kili and Oin (Bbg 17), the sediment is partly much coarser (23 to 5004 µm) and alternates more frequently between silty (up to 85wt%) and gravelly (up to 40wt%) horizons.

The pH values in pingo Fili (Bbg 9) are relatively basic (9.2-9.9) in the lowest (sediment) section between 25 and 22.4 m depth. Between 22.1 and 14 m depth, in the pingo ice, pH ranges from 7.7 to 8.9 and decrease to values between 6.6 and 7.9 in the uppermost pingo ice between 11 and 1.4 m depth (Figure 7). In the same core segments, the EC values change from 462-2670 µS cm^{-1} and 100-834 µS cm^{-1} to 5-106 µS cm^{-1}, respectively. The three core segments can also be identified in the anion data. In the lower core segment, HCO_3^- is 56-83%. In the middle core, the content ranges from 73% to 81%, and in the upper part of the core, it ranges from 17% to 74%. The cation content is very strongly Na+-dominated (96-99%) between 25 and 14 m depth. From 11 to 1.4 m depth, a high K^+ content is observed (11-82%). In the uppermost part of Pingo Fili (0-1.2 m depth), studied in core Bbg 14, the pH values are between 6.3 and 7.9, and the EC values 52-267 µS cm^{-1}. The cation composition is also Na^+ dominated (83-95%) while the anion contents are shared between Cl^- (10-36%), SO_4^{2+} (23-59%), and HCO_3^- (15-64%).

https://doi.org/10.5194/egusphere-2026-1377
Preprint. Discussion started: 12 June 2026

In the slope core Bbg 10 of pingo Fili, the pH values range from 6.7 to 7.9, and the EC values range from 22 to 436 µS cm–1, with a downward trend. Except for the uppermost sample (0.1-0.3 m) with higher Ca^{2+} (36%) and high HCO_3^- content (70%), the cation composition is mainly characterized by Na^+ (55-89%) and K^+ (10-32%), while the anion composition is spread between Cl^- (10-28%), SO_4^{2+} (34-78%) and HCO_3^- (11-47%).

In core Bbg 15 (pingo Kili), the pH values are between 7.0 and 8.5, and EC values are between 27 and 385 µS $cm^{-1,}$ except for the uppermost sample (0-0.3 m depth) with 3650 µS cm^{-1}. The cation composition is Na^+ dominated (79-98%) in the lower core segment (13.8-7.1 m), contains less Na^+ (28-61%) and more K^+ (22-47%) in the middle segment (6.5-4.2 m), and is relatively distributed between Na^+ (54-71%) and K^+ (16-36%) in the upper segment (2.4-0.9 m). The anion composition also alternates between HCO_3^-- dominated (21-77%) in the lower segment, SO42–- dominated (64-90%) in the middle segment, and again HCO3–- dominated (59-77%) in the upper segment. The uppermost samples are dominated by Na^+ (81%) and HCO_3^- (84%).

In core Bbg 11 (north of pingo Kili), the pH values range from 6.9 to 7.6, and the EC values range from 14 to 176 µS cm–1, with a decreasing trend upwards. The cation composition, including Na^+ (27-94%), K^+ (6-25%), Ca^{2+} (12-42%), and Mg^{2+} (6-17%), is highly variable across only four analyses. Similarly, the anion data vary with Cl^- (2-14%), SO_4^{2-} (21-63%), and HCO_3^- (29-63%).

The core Bbg 17 (located between the pingos Kili and Oin) has pH values ranging from 6.8 to 8.8, which increase with depth, and a low electrical conductivity (87-254 µS cm^{-1}). The cation composition is relatively well spread between Na^+ (19-76%), K^+ (12-23%), Ca^{2+} (3-44%), and Mg^{2+} (1-17%). The anion composition is divided between SO_4^{2-} (35-91%) and HCO_3^- (8-61%).

https://doi.org/10.5194/egusphere-2026-1377
Preprint. Discussion started: 12 June 2026

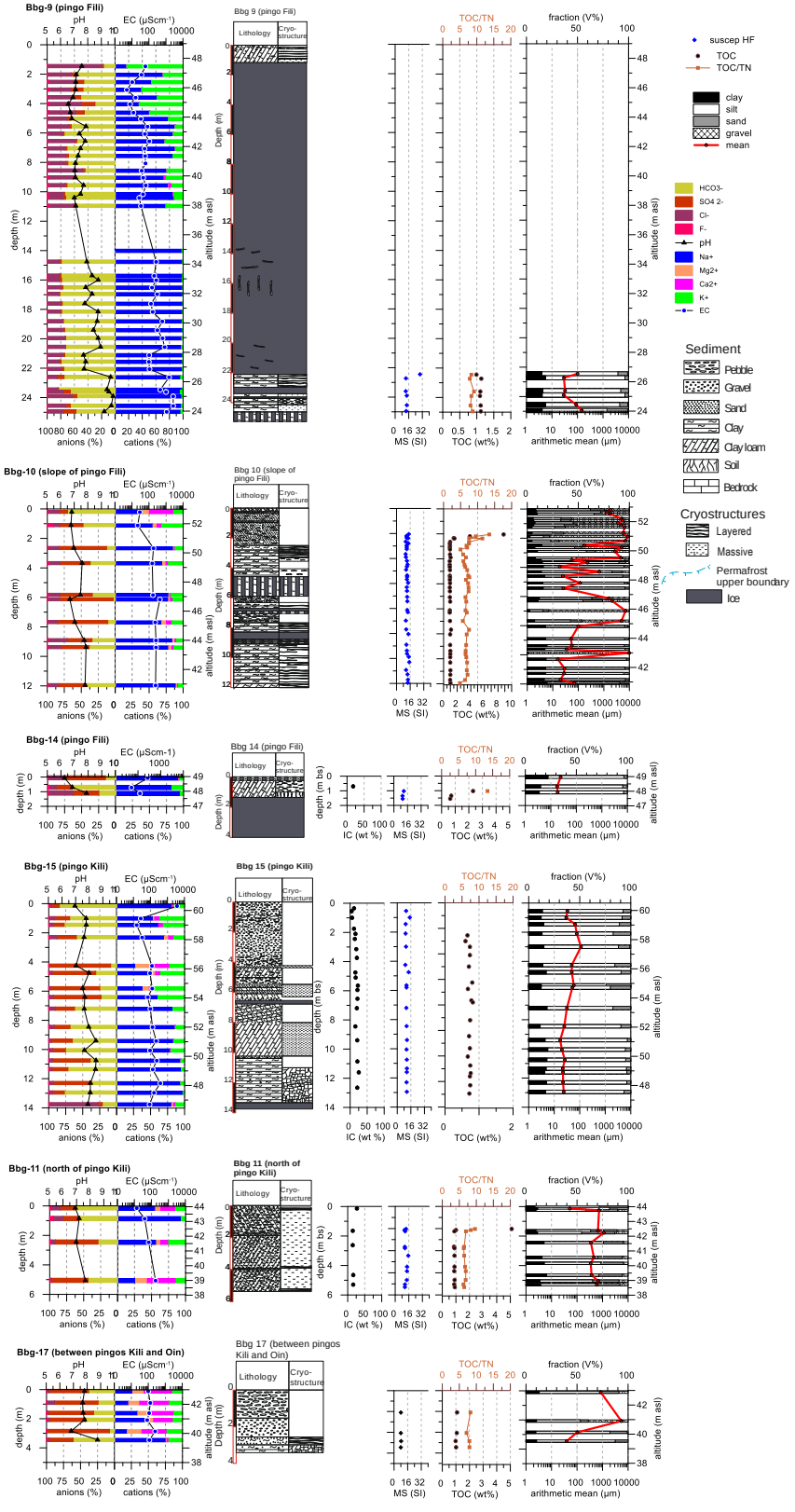

https://doi.org/10.5194/egusphere-2026-1377
Preprint. Discussion started: 12 June 2026

Figure 7 Cryolithological profiles, hydrochemical and sedimentological data from the sub-area C2 (B) (middle part of the Grøndalen Valley).

4.5 Sub-area D (Hollendardalen Valley)

In the Hollendardalen Valley, one core (Bbg-20) was drilled on top of a hill at about 6.5 km north of pingo Nori and 6.8 km east of Kap Finniset (Figure 1, Table 1). The 12 m long core consists in the lowermost part (4.9-12 m depth) of gray-brown loam with gravel and single pebbles and a nesting cryostructure (Figure 8, Table S1.5). Further up (1.8-4.9 m depth), gravel dominates over the finer-grained fractions. The cryostructure is porous. The uppermost part (0.1-1.8 m depth) consists of brownish-gray loam with large amounts of gravel and crushed stones and a nesting cryostructure. Finally, the 0.1 m-thick vegetation cover was drilled at the pingo surface.

In core Bbg-20, the absolute ice content ranges between 11 and 34 wt% (Figure 8). The MS values are between 9 and 13 $10^{-8}m^3kg^{-1}$. The TOC values are somewhat higher (1.0-1.4wt%) between 12.0 and 5.0 m depth. In the upper section (5.0-0.8 m depth), the TOC values range from 0.3 to 0.7wt%. TOC/TN ratios are quite low throughout the core, ranging from 2.1 to 7.0. The $\delta^{13}C$ values are between –29.93 and –26.15 ‰ and thus much lower than in most other core samples. The arithmetic mean grain size ranges from 68 to 7.5 µm. The dominant fraction is silt (67-88wt%) except for a gravel horizon at 3.2-3.0 m depth.

The pH values range from 6.5 to 7.7, and the EC values range from 66 to 272 µS cm^{-1}. The anion composition is distributed between Na^+ (10-50%), K^+ (13-27%), Ca^{2+} (15-47%), and Mg^{2+} (8-28%). The anions are SO_4^{2-} dominated (83-93%) in a lower core segment (12-5 m) and contain lower SO_4^{2-} (40-79%) and more HCO_3^- (15-55%) in an upper segment (4.5-0.8 m).

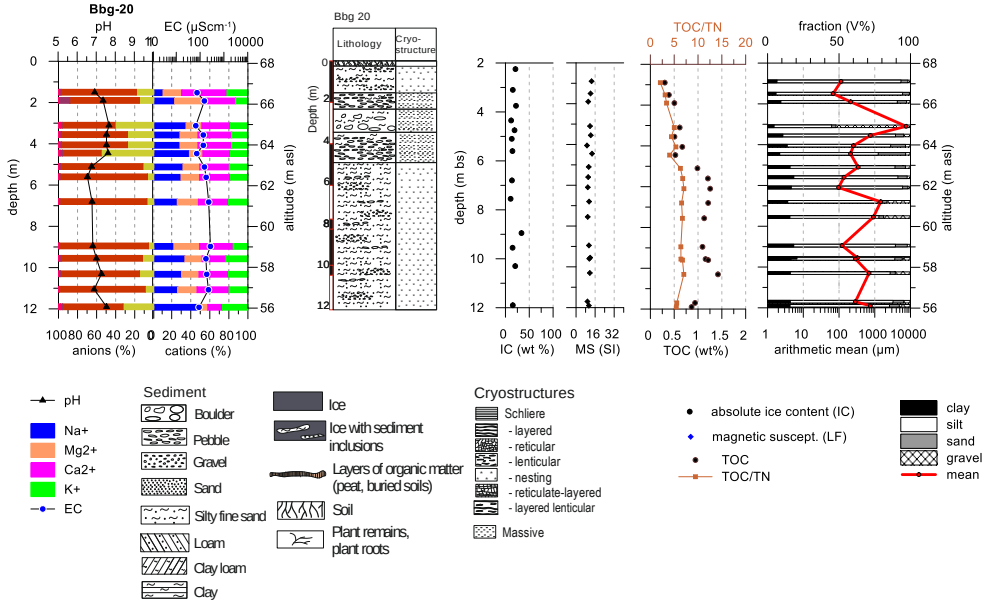

Figure 8 Cryolithological profiles, hydrochemical and sedimentological data from the sub-area D in the Hollendardalen Valley.

https://doi.org/10.5194/egusphere-2026-1377
Preprint. Discussion started: 12 June 2026

4.6 Radiocarbon dating

In total, 63 samples from the cores Bbg 2, 6, 7, 8, 9, 10, 13, 14, 15, 16, 19, the exposure GD 1, and one additional surface sample (T1) were radiocarbon-dated (Table S2; Figure 8).

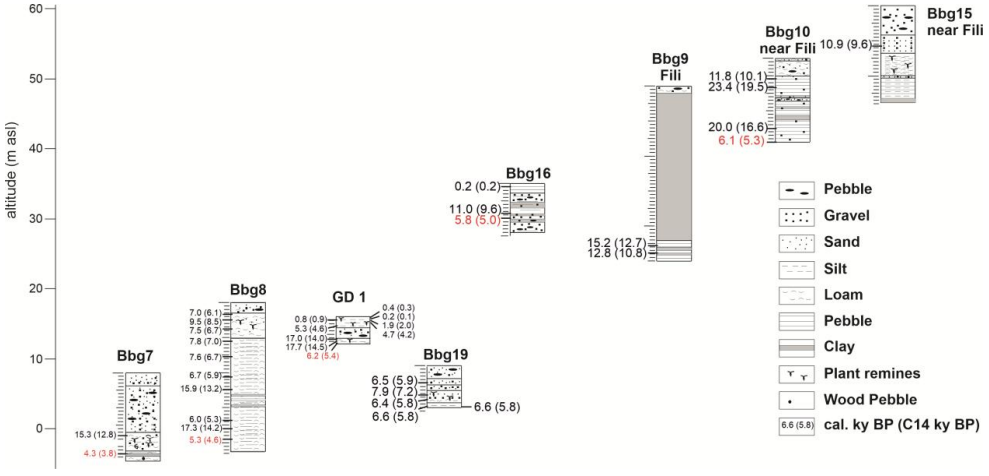

Figure 9 Cryolithological profiles and the used AMS radiocarbon dates (see Table 2) in Grøndalen boreholes and the outcrop GD-1 (red color - age inversions) .

The age values fall within the late Pleistocene and Holocene (Figure 9, Table 2). The distribution of these values across the depths of most cores (Bbg 6, 7, 8, 9, 10, 13, 15, 16, 19) and in the exposure GD 1 shows age inversions, and many values are at the limit of radiocarbon dating reliability (Table S2). From the sub-area A of the marine terraces at the Isfjorden, radiocarbon data were obtained from Bbg 2 and Bbg 6. The data for Bbg 2 are modern, with depths of 2.1 m and 5.1 m. The age of the Bbg 6 core at 1.7 m depth is 21060±50 yr BP. In the sub-area B at Kap Finneset, the core Bbg 7 was dated at several depths. The dating of bulk samples ranges from about 35.7 to 23.1 kyr BP. Two other dates show an inversion, with 15350 cal yr BP at 8.9 m depth and 4295 cal yr BP at 11.6 m depth. In the sub-area C1 at the mouth of the Grøn River, core Bbg 8 is dated between 17243 and 5344 cal yr BP. However, several inversions occur in the age-depth relationship. Between depths of 1.85 and 10.58 m, the sediments can be assigned to the Middle Holocene. The deeper samples up to 17.9 m are partly older (17.2-16 cal kyr BP) and partly younger (6.1 cal kyr BP (Table 2). The nearby located 3.5 m deep exposure GD 1 has a reasonable age-depth relationship spanning from 17690 cal yr BP at 3.33 m depth to 360 cal yr BP in 0.12 m depth. However, there are some minor age inversions here as well. In the middle reaches of the Grøndalen Valley, in sub-area C2, within pingo Fili, the lowest deposits in core Bbg 9 were dated to between 15150 cal yr BP at 22.73 m and 12840 cal yr BP at 23.9 m. The core Bbg 10 from the southern rim of pingo Fili was dated to modern at 0.37 m, to 6130 cal yr BP at 12.95 m, and to 11770 cal yr BP at 2.9 m, with age inversions again. The core Bbg 16 from the southern edge of pingo Nori was dated to 5790 cal yr BP at 4.9 m and 230 cal yr BP at 0.4 m depth. Radiocarbon ages of bulk samples from the cores Bbg 13, 14, and 15 ranged from 38 to 18 kyr BP.

https://doi.org/10.5194/egusphere-2026-1377
Preprint. Discussion started: 12 June 2026

Table 2 Radiocarbon dating results of picked plant material used for interpretation (the complete dataset is documented in Table S2); GD 1 data according to Soloveva et al. (2026); marked in italics-ages below the reliability, because of the late Pleistocene glaciation

Lab no.	Sample Label	mean depth (m)	age (yr BP)	±(yr)	cal yr BP (2 σ) from	cal yr BP (2 σ) to	cal yr BP mean
AWI 2885.1.1	Bbg 7/5	890	12844	105	15047	15658	15350
AWI 2886.1.1	Bbg 7/6	1160	3885	74	4140	4449	4290
AWI 2876.1.1	Bbg 8/9	185	6124	51	6882	7165	7020
IGAN 5869	Bbg 8/15	26	8500	30	9473	9538	9510
AWI 2877.1.1	Bbg 8/17	375	6674	52	7431	7617	7520
AWI 2878.1.1	Bbg 8/21	555	7025	54	7725	7963	7840
AWI 2879.1.1	Bbg 8/23	775	6720	59	7478	7676	7580
AWI 2880.1.1	Bbg 8/30	1058	5860	82	6450	6883	6670
AWI 2881.1.1	Bbg 8/34	124	13248	55	15721	16097	15,910
AWI 2882.1.1	Bbg 8/38	1685	5307	79	5927	6220	6070
AWI 2883.1.1	*Bbg 8/41*	*17,90*	*14208*	*63*	*17078*	*17411*	*17250*
AWI 2884.1.1	Bbg 8/46	1950	4612	72	5207	5480	5340
AWI 9191.1.1	Bbg 19 2.4-2.5	245	5856	50	6503	6516	6510
AWI 9192.1.1	Bbg 19 4.2-4.4	43	7164	54	7919	8043	7980
AWI 9193.1.1	Bbg 19 5.0-5.2	51	5784	61	6443	6415	6430
AWI 9194.1.1	Bbg 19 5.8-5.9	585	5797	52	6485	6736	6610
AWI 9195.1.1	Bbg 19 6.0-6.2	61	5780	93	6392	6792	6590
IGAN5195	GD-1_0.07-0.17	012	275	30	283	443	360
IGAN5196	GD-1_0.17-0.35	026	140	30	50	279	160
IGAN 5197	GD-1_0.50-0.58	054	920	40	768	916	840
IGAN 5198	GD-1_0.58-0.66	062	1990	80	1721	2122	1920
IGAN 5180	GD-1_0.66-0.67	0665	4160	60	4527	4837	4680
IGAN 5182	GD-1_1.10-1.15	130	4600	60	5214	5471	5340
$IGAN_{AMS*}5183$	*GD 1 3.15-3.20*	*3175*	*13995*	*40*	*16880*	*17129*	*17000*
$IGAN_{AMS*}5184$	*GD 1 3.20-3.45*	*3325*	*14520*	*40*	*17460*	*17912*	*17690*
IGAN5185	GD 1 3.45-3.70	3575	5440	280	5596	6797	6200
AWI 2561.1.1	Bbg 9/4	2390	10814	121	12615	13069	12840
AWI 2560.1.1	Bbg 9/2	2273	12665	130	14784	15512	15150
AWI 2633.1.1	Bbg 10/14C	037	modern	-	-	-	
AWI 2634.1.1	Bbg 10/13	290	10133	58	11597	11940	11770
AWI 2635.1.1	*Bbg 10/18*	*430*	*19510*	*220*	*22987*	*23879*	*23430*
AWI 2636.1.1	*Bbg 10/29b*	*988*	*16616*	*172*	*19602*	*20459*	*20030*
AWI 2637.1.1	Bbg 10/34	1195	5353	120	5902	6355	6130
AWI 9888.1.3	Bbg 15 5.7-5.9	58	9583	103	10653	11198	10930
AWI 2561.1.1	Bbg 16 0.3-0.5	04	218	51	132	327	230
AWI 9887.1.1	Bbg 16 4.2-4.3	425	9626	109	10678	11235	10960
AWI 2560.1.1	Bbg 16 4.8-5.0	49	5043	90	5596	5984	5790

4.7. Paleo-ecological studies from outcrop GD-1

Samples from the outcrop GD-1 have been analyzed for spores, pollen, and diatoms to deduce postglacial ecological conditions (Soloveva et al., 2026)

https://doi.org/10.5194/egusphere-2026-1377
Preprint. Discussion started: 12 June 2026

According to spores and pollen data, the GD-1 sequence differentiates into the pollen zones 1, 2a-c, 3, and 4. The almost complete absence of microfossils in pollen zone 1 (370-120 cm depth, 17.6 to 6.2 cal kyr BP) may be due to both scarce vegetation, low plant productivity, and the predominance of vegetative reproduction in extremely harsh climates. Subzone 2a (115-95 cm depth, 5.3 cal kyr BP) reflects the development of sedge-grass moss tundra with shrubby willows and birches. Subzone 2b (95-58 cm depth, 4.7 to 1.9 cal kyr BP) was characterized by monodominant communities from representatives of the sedge family. In subzone 2c (58-35 cm depth, 0.8 cal kyr BP), shrub species such as polar willow and dwarf birch reappear in herbaceous sedge plant communities. Low spore and pollen contents in zone 3 (35-17 cm depth, 0.2 cal kyr BP) and the abundance of Pre-Quaternary microfossils indicate unfavorable conditions during this stage. The abundance of willow and grass pollen in zone 4 (17-0 cm depth) reflects the modern vegetation of grass and willow tundra.
The diatom record of outcrop GD-1 divides into five diatom zones. In diatom zone 1 (345-315 cm depth, 17.6 to 17 cal kyr BP), single freshwater diatoms and shell fragments of marine diatoms were found. At a depth of 315-310 cm, few benthic freshwater diatoms were found. A shallow paleo-water reservoir may have existed. The diatom zone 2 (155-140 cm depth) was dominated by benthic acidophilic freshwater diatoms from a very shallow freshwater reservoir with some input of aerophilic and rheophilic species. The diatom zone 3 (140-115 cm depth, 5.3 cal kyr BP) is characterized by a rich benthic freshwater association in a shallow water body with an alkaline environment and a noticeable influx of rheophilic and aerophilic diatom species. The inflow of rheophiles may reflect an increase in river flow due. The diatom zone 4 (67-35 cm, 1.9 to 0.8 cal kyr BP) is dominated by benthic alkaliphilous freshwater diatoms. The diatom association of zone 4 includes marsh species. The diatom zone 5 (17-7 cm depth, 0.4 cal kyr BP) is characterized by the predominance of benthic alkaliphilic freshwater diatoms. The diatom association is similar to zone 4 but is less species-rich.

5. Discussion

5.1 Geochronology

The interpretation of radiocarbon dating results is complicated by the presence of fossil carbon from the surrounding Tertiary coal deposits (Marshall et al., 2015; Orheim et al., 2007). This mainly relates to bulk sediment samples in which no plant remains were found. A few samples were dated twice, by bulk and by plant remains. These samples exhibited significant differences, as seen in sample Bbg 7/6, which had a bulk age of 35442 cal yr BP and a plant-fragment age of 4295 cal yr BP (Table S2). Therefore, we prioritized ages based on single-plant remains for subsequent interpretation. Furthermore, we restrict our interpretation to ages younger than 16 cal kyr BP, i.e., after regional deglaciation, yielding 30 dates spanning from 14784 cal yr BP to the present (Table 2).
As shown in Table 2, Table S2, and Figure 9, the obtained radiocarbon dates span a wide range, from the late Pleistocene to the late Holocene. In principle, the oldest dates can be relevant and correspond to deposition in the valley floor that occurred during the later stages of the late Weichselian glaciation - in a dry or lake-filled ice-dammed oasis that appeared due to local glaciers' mass balance disparity (Demidov and Terekhov, 2024), or during the middle Weichselian interstadial (Salvigsen and Nydal, 1981) or the Leinstranda interglacial (Miller et al., 1989). However, at present, there is insufficient regional research to support this interpretation.
According to Mangerud and Svendsen (1990) and Svendsen and Mangerud (1992), the area of Lake Linnévatnet (west of the Grønfjorden) was deglaciated around 12,300±190 yr BP. (14.4 cal kyr BP). Mangerud and Svendsen (2018) interpreted sediment records from Lake Linnévatnet, indicating glacier retreat between 11 and 10 cal kyr BP. The oldest marine mollusk age in the area dates to 11.7 cal kyr BP (Sharin et al., 2014), suggesting deglaciation by then (Farnsworth et al., 2020a, b). According to Mangerud et al. (1992), at the southern coast of the Bellsund, about 40 km south of the Grøndalen

https://doi.org/10.5194/egusphere-2026-1377
Preprint. Discussion started: 12 June 2026

study area, the oldest shells were dated 13.27±0.210 kyr BP (16.01 to 14.45 cal kyr BP). All dates older than 16 cal kyr BP are therefore excluded from further interpretation. The older ages obtained in the present study (see Figure 9 and Table S2) most likely result from mixed, co-dated older organic fossil carbon derived from adjacent Tertiary coal deposits (Marshall et al., 2015; Orheim et al., 2007). Similar observations in a comparable geologic setting were reported by Kusch et al. (2021), confirming the influence of ancient coal-derived organic carbon on the $\delta^{13}C$ and $\delta^{14}C$ values of organic carbon in soil and sediments in the Bayelva River catchment near Ny-Ålesund.

A second challenge with radiocarbon dating in the study region is the occurrence of multiple age inversions in individual samples across all cores and the outcrop. These results are attributed to plant material transported from the active layer by cryoturbation – a common periglacial process (Gentsch et al., 2015, Wetterich et al., 2014) before the material entered a perennially frozen state, or to organic material carried down during drilling, both of which are possible explanations for the young ages at greater depths. In contrast, high ages at lower depths probably stem from admixtures of old tertiary carbon. Finally, many of the drilled layers are quite coarse-grained with very low organic content.

The interpretation of the datable material can be primarily summarized as an overview of all cores and the outcrop. Six dates fall between 15 cal kyr BP and 9.5 cal kyr BP. Most of the dates (18) fall within the age range of approximately 8-4 cal kyr BP. Five samples from the uppermost layers have been dated between 1.7 and 0.2 cal kyr BP.

5.2 Summary and comparison of sediment data

Generally, grain-size data are highly variable across the studied cores, ranging from a mean grain size of 11 to 9784 µm, and represent clayey silt to gravelly sand deposits (Figure 10).

In sub-area A at the Isfjord terraces (Figure S3.1), smaller medium sand grain sizes and larger proportions of clay and silt provide evidence of alluvial or marshy depositional conditions on the marine fjord terraces, while higher medium grain sizes and larger sand and gravel contents prove more intense movement during deposition.

In sub-area B (Kap Finneset at the Grønfjord), high silt and clay contents reflect quiet depositional conditions in most core sections. Only the higher gravel content and coarser grain sizes in the upper section provide evidence of fluvial or beach accumulation and more intense movement at the fjord shore (Figure S3.2).

The sedimentological results at the mouth of the Grøn River (sub-area C1) prove, on one hand, calm depositional conditions with small mean grain sizes and high clay and silt fractions for most of the core Bbg 8. In cores Bbg 18 and Bbg 19, however, clearly coarser fractions with sand contents between 8 and 36wt% and gravel contents of 5 to 32wt% are present. This suggests repeated fluvial deposition, alternating with periods of calmer conditions. This is common in the delta area of a river or deposition from a debris cone (Figure S3.3).

The pingo core Bbg 13 of sub-area C2A consists of both below and above the pingo massive ice, predominantly of clayish-silty material. 80 m south of the pingo top, the sediments of core Bbg 16 show clear alternations of silty-sandy gravel with clayish silt. This is typical for a small delta or from a debris cone that probably reached from the south toward the Grøn River (Figure S3. 4).

The cores from sub-area C2B exhibit the widest range of grain-size distributions. The sediments of the pingos Fili and Kili (Figure S3.5) are again clayish silt, while on the slope of a pingo, alternations of sandy-gravelly and clayey-silty sediments are typical. The sediments in the Grøn River floodplain and directly in the river are characterized by silty sand and gravelly sand, respectively. Only some of the horizons from core Bbg 10 have very high contents (> 70wt%) of sand and gravel (Figure 10).

The material from the hill in Hollendardalen Valley (sub-area D, Figure S3.6) is much coarser than that of the pingo cores studied and consists of sandy silt and gravelly-sandy silt.

https://doi.org/10.5194/egusphere-2026-1377
Preprint. Discussion started: 12 June 2026

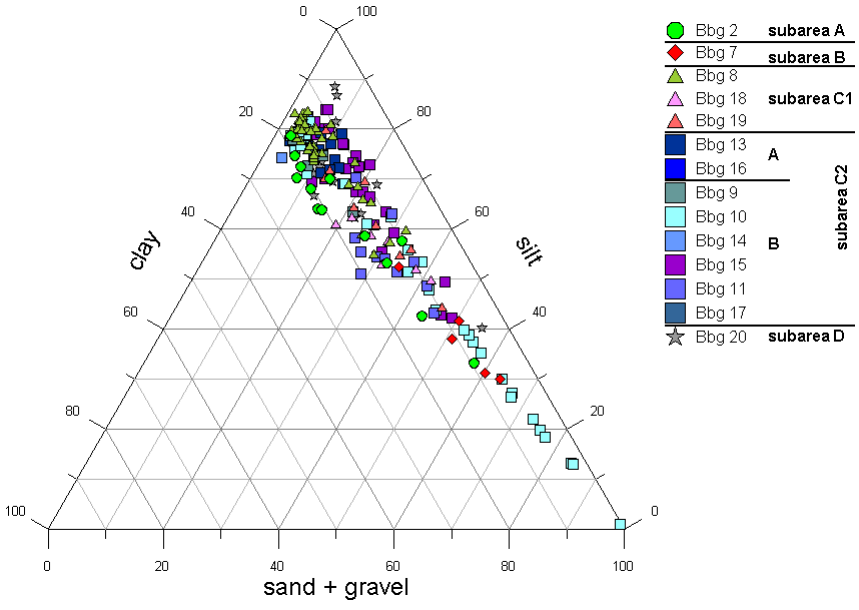

Figure 10 Clay – silt – (sand + gravel) diagram of all studied cores showing a wide range from coarse-grained sandy gravelly (fluvial or marine beach) to fine-grained silty (alluvial) deposits.

There are relatively small differences between the study sites in biogeochemical data and mass-specific magnetic susceptibility. The TN values are mostly between 0.1 and 0.2wt%. Only in the uppermost cm (within the vegetation cover) of the cores do values of up to 0.66wt% occur.

The TOC ranges from 0.3 to 8.8 wt%. Values> 2 wt% were measured exclusively in the vegetated topsoils. The TOC/TN ratio, a measure of organic matter decomposition, ranges from 2 to 15. Values significantly greater than 11 are again limited to the rooted top-soils and a slightly organic-rich horizon in Bbg 16. These relatively close ratios provide evidence of higher decomposition of organic matter (e.g., Schirrmeister et al., 2011) and the occurrence of ancient organic matter from the adjacent Tertiary coals.

The $\delta^{13}C$ values range from –29.9 to –24.2‰. In the sub-areas A, B, and C1, they are very close to each other, ranging from –26.4 to –24.3‰. In sub-area C2, only two samples are < 27‰. This finally provides a very narrow range in the TOC/TN- $\delta^{13}C$ diagram (Figure 11). Only the core Bbg 20 on a hill in the Hollendardalen Valley shows lower $\delta^{13}C$ values between –29.9 and –26.2‰.

The mass-specific magnetic susceptibilities in the cores are also very similar, ranging from 6.4 to 17.0 $\times 10^{-8}$ m^3 kg^{-1}. Only three samples in cores Bbg 8 and Bbg 19 have values greater than 20 x 10^{-8} m^3 kg^{-1}. This means that the mineralogical composition of the original parent rock remained unchanged during its depositional history.

https://doi.org/10.5194/egusphere-2026-1377
Preprint. Discussion started: 12 June 2026

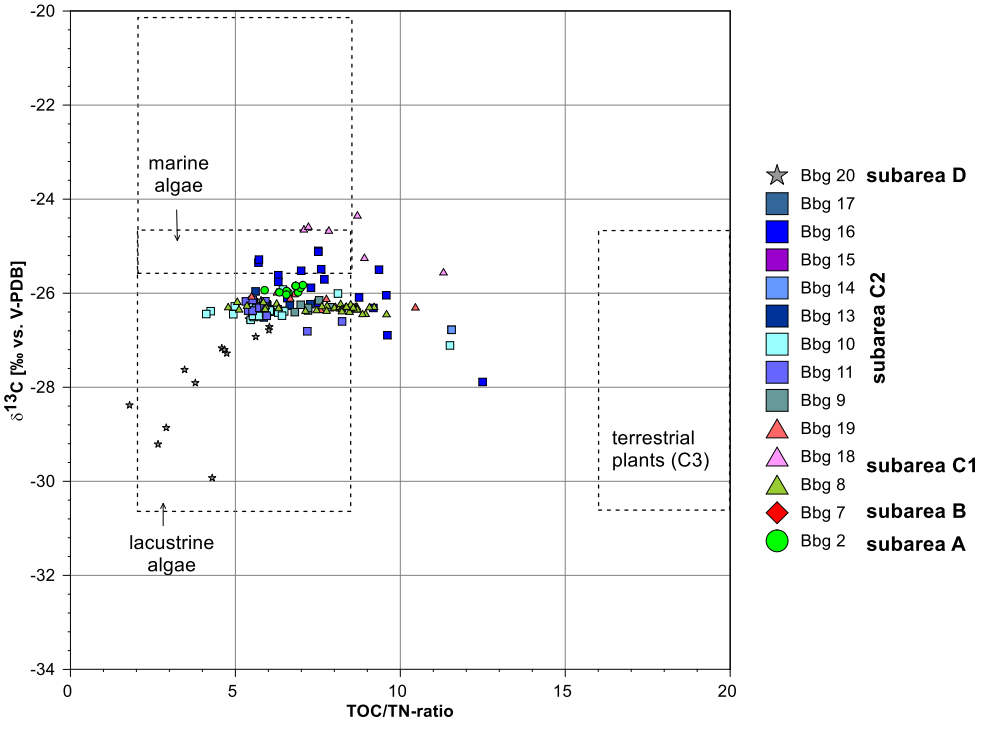

741

742 Figure 11 The TOC/TN -$\delta^{13}C$ diagram of all studied cores showing a very narrow data range.

743

744 **5.3 Hydrochemical data**

745 Water extracts from sediment samples and water data from pingo ice indicate the origin of the frozen
746 water and the amounts of soluble compounds. To summarize the data from the 293 analyses, a Piper
747 plot (Piper, 1944) was used.
748 Salinization may play a significant role in explaining the observed hydrochemical characteristics in the
749 Barentsburg area. In northern Germany, groundwater salinization results from brines in the deeper
750 subsurface. An empirical method was developed by Rechlin (2008) and Lehmann (1974a, b) to detect
751 and control the onset of salinization by intervening in the production regime of groundwater wells.
752 The method is based on water types, as described by Valyashko (1962). Although this method refers
753 to hydrochemical processes that occur after halite precipitation, it is highly sensitive to changes in
754 freshwater. The reason is that the ion pair Ca2+-HCO_3^+, which is dominant in freshwater, is not
755 considered. Thus, changes in the remaining ions are more accurately noticed. The basic genetic ratio
756 (GGV) and the saline matrix coefficient (Salinar Matrix Koeffizient, SMK) were developed (Rechlin,
757 2008; Brose, 2017), which helps to consider the influence of saltwater more precisely. The GGV ratio
758 was initially defined as the KCl/NaCl ratio and later extended to the K-salts/(NaCl + NaBr +NH_4Cl +$FeCl_2$)
759 ratio. A GGV ratio smaller than 0.5 indicates an initial marine influence. The smaller the ratio, the
760 stronger the influence of salinization. In the SMK ($NaHCO_3$+$MgSO_4$+$MgCl_2$+K-salts+NH_4-salts+NO_3-salts)
761 / ($CaCl_2$+NaCl+NaBr), the relation of "freshwater salts" to "saltwater salts" is shown. If the ratio is below
762 1, a saltwater influence is assumed.
763 The ion composition of water extracts of core Bbg 2 from the Isfjord terraces (sub-area A) almost
764 corresponds to the sodium-chloride type in the Piper plot, which points to the still preserved marine

https://doi.org/10.5194/egusphere-2026-1377
Preprint. Discussion started: 12 June 2026

origin of the soil moisture (Figure 12). However, only from 2.7 m depth in borehole Bbg 2 and 3.7 m in Bbg 5, higher conductivity values (200-1200 µS cm^{-1}) are present, which support even more a marine water origin (Figure 3). In the cation diagram, almost all samples fall within the sodium-potassium field, with sodium predominating in the samples by 65-90% at high electrical conductivities (Figure 12). The anion diagram does not show such a clear assignment. Water extracts of the sulfate and chloride type occur as well as those in the non-dominant field. However, the GGV ratio of Bbg 2 at a depth of 7 to 2.38 m ranges from 0.06 to 0.49, and the SMK ratio at a depth of 2.38 to 3.2 m ranges from 0.4 to 0.9; both ratios indicate a clear marine influence on the hydrochemical composition of the ground ice in sub-area A.

At Kap Finneset (sub-area B), the water extracts of core Bbg 7 are in the sodium chloride field of the diamond diagram or at its edges, comparable to the ionic compositions in sub-area A (Figure 12). However, only the EC data from a depth of 10.8 m show somewhat higher values (430-830 µS cm^{-1}, Figure 4). The lower deposits at the Grønfjorden terrace may not have been washed out by the Grøn River. In the cation diagram, almost all samples are in the sodium-potassium field, but more broadly distributed than in sub-area A (Figure 12). In the anion diagram, all fields are occupied by data points (Figure 11). The high GGV and SMK ratios exclude a marine influence in sub-area B.

At the mouth of the Grøn River (sub-area C1), the water extracts of the cores Bbg 8, 18, and 19 have mostly very high electrical conductivities of about 1000 to 12,000 µS cm^{-1} (Figure 4). In the uppermost core meter (up to 1 m depth) and in a section between 12.6 and 14.7 m depth in Bbg 8, there are lower conductivities. The values are again located in the sodium chloride field of the diamond diagram (Figure 11). For the cations, the values are concentrated primarily in the sodium-potassium field. For the anions, they are in the chloride field due to the frequently high chloride content of 50-90%. The GGV (0.03 to 0.6) and SMK (0.01 to 0.93) ratios are low or very low in most samples. That reflects the influence of seawater and cryo-pegs formed from seawater (Demidov et al., 2020).

In the middle reaches of Grøndalen Valley (sub-area C2(A)), partly higher electrical conductivities are found in the ice of Pingo Nori (Bbg 13; 900 to 5400 µS cm^{-1}) and also in the underlying sediment (Figure 5). In the anion diagram, the water data from the pingo ice and the underlying sediment are located in the chloride field. In the cation diagram, they are positioned very close together in the sodium-potassium field, and correspondingly, in the sodium-chloride field in the diamond diagram (Figure 12). For Bbg 13, the GGV ratio is already low at a depth of 0.25 m (0.21) and remains very low (0.01 to 0.1) at depths of 2.38 m and deeper. The SMK ratio is < 1 at 0.25-0.4 m depth and deeper, reaching 2.38 m. All these data again reflect the influence of a cryopeg formed from seawater during pingo formation. The core from the edge of the pingo (Bbg 16) has low conductivities (20-94 µS cm^{-1}), while the data scatter widely in the chloride field of the cation diagram and are spread over the entire range in the anion diagram (Figure 12).

In sub-area C2(B) of the Grøndalen Valley, slightly higher conductivities (100-830 µS cm^{-1}) were measured in the lower section of the ice from pingo Fili (core Bbg 9) at 14 to 22 m depth and in the sediment below the ice at 22.4-25 m (460-2700 µS cm^{-1}) and in the uppermost sample (0.0-0.3 m) from core Bbg 11 in Pingo Kili (3650 µS cm^{-1}, Figure 6). The GGV ratio in Bbg 9 is < 0.5 from 5 m depth, but the SMK is almost > 1, and the electrical conductivity is small to 11 m depth. From this, a low marine influence for the upper section, a stronger influence for the middle section, and a strong marine influence for the lowest section can be interpreted. The electrical conductivities of the other cores' water extracts are significantly lower (7 to about 300 µS cm^{-1}). In the Piper plot (Figure 12), the anion data for the pingo ice are predominantly in the bicarbonate field and at its margins. The cation data range from the sodium-potassium field to the non-dominant central field. Therefore, the values in the Piper plot fall within the lower range of the sodium chloride or sodium bicarbonate field, or are distributed more widely across the diagram. The values from the other cores in the pingo margin (core Bbg 10), on the floodplain (core Bbg 11), and in the riverbed sediment (core Bbg 17) are widely

https://doi.org/10.5194/egusphere-2026-1377
Preprint. Discussion started: 12 June 2026

distributed in the anion diagram and similarly distributed in the cation diagram as the data from the pingo ice. Accordingly, values are present in all four fields of the Piper plot. Although the electrical conductivities for Bbg 10 are relatively low, a small but clear marine influence can be interpreted from GGV values between 0.25 and 0.45.

In the Hollendardalen Valley (sub-area D), the electrical conductivity is low (70-270 µS cm^{-1}, Figure 8). The cation values are in the non-dominant central field, and the anion data are in the sulfate field. In the diamond diagram, they are almost in the calcium chloride field (Figure 11). This is a considerably different picture than for all other cores.

From the discussion of the presented water analysis data, it can be concluded that the ice and the water extract have low electrical conductivities, relatively low anion and cation values, and a wide spread in the Piper plot, suggesting a terrestrial origin. High conductivities and high sodium-chloride composition indicate marine and/or cryopeg influence.

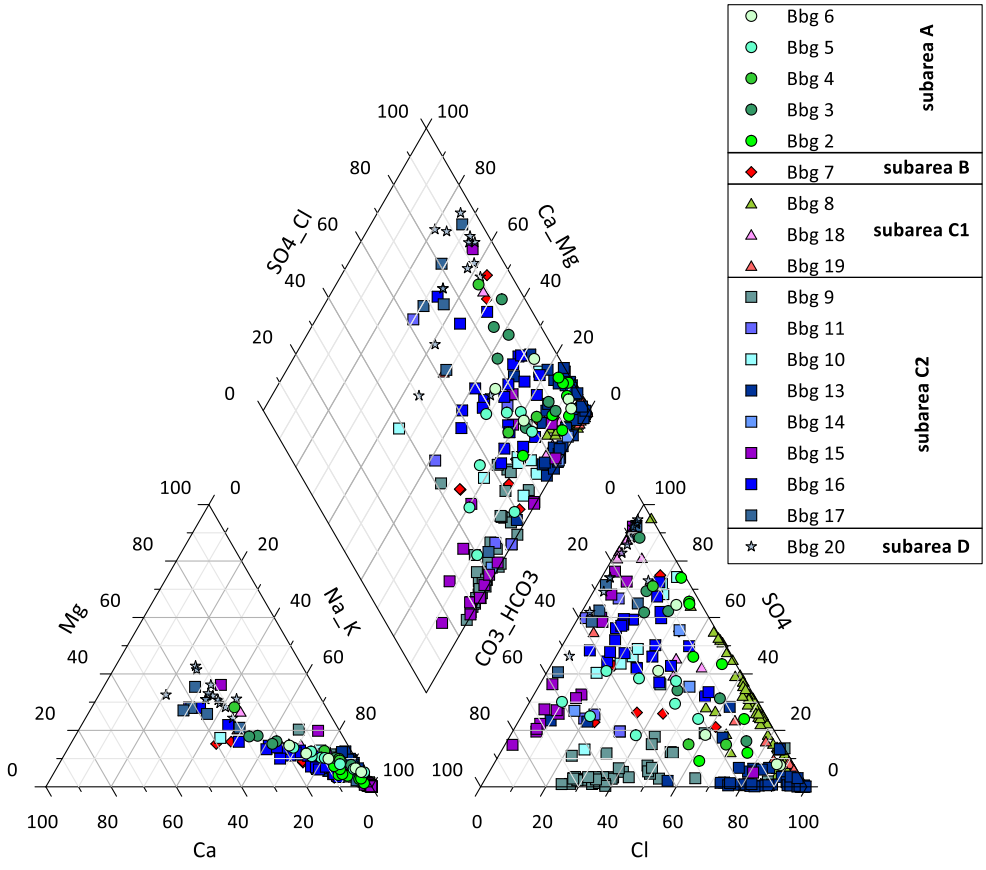

Figure 12 Hydrochemical Piper plot of all permafrost deposits, water extracts, and pingo ice showing in the diamond graph Na-Cl, but also Ca-Mg-SO_4 and sometimes Na-HCO_3 dominance, mostly Na+K dominance for cations, and no specific focus for anions.

Regarding the periods with higher electrical conductivity and a possible stronger influence of marine water, no clear picture emerges. Water extracts and ice samples with higher conductivities in dated

https://doi.org/10.5194/egusphere-2026-1377
Preprint. Discussion started: 12 June 2026

cores (Bbg 7, 8, 19, 13) are distributed over the interpretable period from ca. 11 to 4.1 cal kyr BP. Salty water may therefore have penetrated sediments of different ages.

5.4 Landscape history after deglaciation

The data from the present study, obtained along a drilling transect across the coastal areas at the Isfjorden shore into the Grøndalen and Hollendardalen valleys, cover a large portion of the modern landscape inventory that formed over the last approximately 12,000 years following deglaciation on West Spitsbergen. When combined with the literature, three main stages of landscape evolution can be distinguished (Table 3).

The termination of the Lateglacial to early Holocene deglaciation period in the region (stage 1) is inferred indirectly from the oldest marine-fossil dates, which may have been deposited only after glacial retreat during marine transgression. In the study region of Nordenskiöld Land, such data span from 14.4 cal kyr BP (Mangerud and Svendsen, 1990; Svendsen and Mangerud, 1992) to 11.7 cal kyr BP (Sharin et al., 2004), while the oldest postglacial lacustrine deposition of Lake Linnévatnet indicates a glacier retreat between 11 and 10 cal kyr BP (Mangerud and Svendsen, 2018).

Further-dated marine shells and whalebones represent marine transgression (stage 2) between 11.2-10.7 cal kyr BP, reaching maximum altitudes of 64 m asl, and 7.1-6.4 cal kyr BP, reaching 12.5 m asl in Nordenskiöld Land (Landvik et al., 1987, 1998). Will be great to add: According to the study by Kriauchunas et al. (2020), the deposits at Kap Finneset were formed in a marine delta environment around 8 cal kyr BP (marine regression). In the present core data, traces of marine deposition are seen in ion composition with domination Na-Cl, high ionic content of EC >1 mS cm^{-1} in the lower part of core Bbg 2 (< 70.5 m asl) at the Isfjord terraces (sub-area A), in the cores Bbg 8 (< 17 m asl), Bbg 18 (< -1 m asl) and Bbg 19 (< 7 m asl) in the lower reaches of the Grøndalen Valley (sub-area C1), and the lowermost parts of core Bbg 9 (< 26.4 m asl) and Bbg 13 (< 28.4 m asl) in the middle part of the Grøndalen Valley (sub-area C2). The marine signature in hydrochemical parameters also indicates the formation of cryopegs and saline groundwater aquifers influenced by former seawater.

The terrestrial deposition and permafrost aggradation (stage 3) differentiate into three landscape-shaping regimes (Table 3). Periglacial fluvial and alluvial deposition (stage 3a, 6.4 to 4.4 cal kyr BP) is characterized by coarser-grained sediments with arithmetic grain-size mean > 500 µm and higher gravel contents (5 to 98wt%), which are partly interbedded with fine-grained sediments with arithmetic mean grain size diameter of 20-150 µm and high silt fractions (50-80wt%). Such parameters are measured in the uppermost part of core Bbg 2 at the Isfjord terraces (sub-area A), in core Bbg 7 at Kap Finneset (sub-area B), in the cores Bbg 18 and single parts of Bbg 19 in the lower reaches of the Grøndalen Valley (sub-area C1), in most parts of the cores Bbg 10, Bbg 11 and single parts of the cores Bbg 16 and Bbg 17 in the middle part of the Grøndalen Valley (sub-area C2), and parts of the core Bbg 20 in the Hollendardalen Valley (sub-area D). According to the paleoenvironmental study by Soloveva et al. (2026) on the GD-1 exposure, a shallow alkaline water body with increased river flow existed around 5.3 cal kyr BP, while the surrounding area was characterized by sedge-grass-moss tundra with shrubby willows and birches. The pollen data indicate warmer conditions than today at 5.3 cal yr BP, but colder conditions at about 4.7 cal kyr BP.

Unfortunately, there are no reasonable radiocarbon dating results for the pingo formation in stage 3b. Where the underlying sediments have been dated, the ages are too old to be interpreted. We assume that pingo formation began after fluvial and alluvial accumulation, i.e., after ca. 4.4 cal kyr BP, in a colder-than-present landscape with aggrading permafrost (pollen Subzone 3b in Soloveva et al., 2026; see also Demidov et al., 2019). The pingo ice is characterized by low electrical conductivities of 5 to 500 µS cm^{-1} in large sections of the cores. In the lower areas closer to the underlying sediments, the influence of former seawater is much stronger, with conductivities of 1000-5000 µS cm^{-1}. There is a

https://doi.org/10.5194/egusphere-2026-1377
Preprint. Discussion started: 12 June 2026

sensible difference in sub-area C2(A) (Bbg 13; pingo Nori; Demidov et al., 2021) and sub-area C2(B) (Bbg 9; pingo Fili; Demidov et al., 2019) pingo ice in terms of overall anion dominance. The anion data for the Nori pingo plot in the chloride field but for the Fili pingo in the bicarbonate field (Figure 11). This demonstrates the stronger influence of former seawater in the lower reaches of the Grøndalen Valley in sub-area C2(A) while its upper reaches in sub-area C2(B) predominantly experienced the influence of terrestrial groundwater after the marine regression.

Slope and alluvial deposition, pingo degradation, and recently observed rapid permafrost disturbances in places (Demidov et al., 2024) represent the latest stage of landscape development in the study area (stage 3c). Only fine-grained deposition occurred in the study subarea. Around 4.7 cal kyr BP, sedge vegetation was dominant in the vicinity of exposure GD-1. According to Soloveva et al. (2026), a shallow alkaline water body was present from 1.9 to 0.8 cal kyr BP, surrounded by polar willow and dwarf birch within herbaceous sedge plant communities. At about 0.2 cal kyr BP, the vegetation composition changed to the modern grass-and-willow tundra.

Because the Arctic and its permafrost have warmed significantly and undergone considerable landscape transformations in recent times, understanding their evolution over geological timescales requires basic research to better understand the interactions between climate and permafrost. In this context, this study provides new data on permafrost's response to late-glacial and Holocene environmental changes on Svalbard. Generally, permafrost studies linking the broad application of several sedimentological, biogeochemical, and paleontological proxies across a landscape scale are rare on Svalbard and, when conducted, are focused on Adventdalen (e.g., Cable et al., 2018; Oliva et al., 2014). Such studies from other regions are, however, necessary to reconstruct postglacial landscape evolution, especially in regions where intense monitoring of modern climate and permafrost is ongoing. Furthermore, most paleo-permafrost studies on Svalbard are restricted to single locations, while a transect approach – as applied in the present study – is largely missing, which is, however, needed to cover the spatial variability of the sedimentation history and periglacial morphology, and to provide background data and understanding for the recent drastic changes in permafrost conditions.

https://doi.org/10.5194/egusphere-2026-1377
Preprint. Discussion started: 12 June 2026

906

907 Table 3 Stages, periods, and indicators of landscape history in the study area

Stage no.	Depositional regime	Time	Indicators	References
3c	Slope and alluvial deposition, pingo degradation, rapid permafrost disturbances	4.7 cal kyr BP until now	Polar willow and dwarf birch, and sedge vegetation changed to the modern grass and willow tundra, with thaw lakes on pingo tops	This study; Demidov et al. (2019, 2020, 2022, 2024), Soloveva et al. (2026)
3b	Pingo formation	Assumed after 4.4 cal kyr BP	Massive pingo ice, frost mound morphology, stable water isotopes with trends characteristic both for open system and closed system fractionation, mostly low ion content (5-500 µS cm^{-1}, < 47.5 and < 37.5 m asl), only high ion content (1 to 5 S/cm, < 28.4 m asl) close to the underlying sediments, sodium chloride ion dominance in the lower valley, sodium bicarbonate ion dominance in upper valley.	This study; Demidov et al. (2019, 2021, 2022)
3a	Periglacial, fluvial, and alluvial deposition	6.4 to 4.4 cal kyr BP	Alternate bedding of coarse-grained (> 500 µm) and finer-grained deposits (20-150 µm); low ion content in water extracts (EC <1 mS cm^{-1}; m asl); shallow alkaline water bodies, sedge-grass moss tundra with shrubby willows and birches	This study; Soloveva et al. (2026)
2	Marine transgression	8 to 7 cal kyr BP	Cryopegs, Na-Cl dominated, high ion content in water extracts (EC < 1 mS cm^{-1}; < 70 to < -1 m asl); redeposited shell fragments of marine diatoms; formation of marine terraces, paleomarine curve from Itterdalen, marine shells at Kap Finneset	This study; Demidov et al. (2020) Soloveva et al. (2026, Landvik et al. (1987), Kriauchunas, et al. (2020)
		11.2-10.7 cal kyr BP (max. 64 m asl), 7.1-6.4 cal kyr BP (12.5 m asl)	Dated marine shells and whalebones	Landvik et al. (1987, 1998)
1	Deglaciation	15-13.8 cal kyr BP (11-10 cal kyr BP)	Dated marine shells above late Weichselian till below Linné Lake, west of Grønfjorden,	Mangerud and Svendsen (1990, 2018); Svendsen and Mangerud (1992), Sharin et al. (2014)

908

https://doi.org/10.5194/egusphere-2026-1377
Preprint. Discussion started: 12 June 2026

Finally, the stages of landscape development in our study area between Isfjorden and Groendalen are compared with those of the Adventdalen Valley, about 40 km to the east. According to Gilbert et al. (2018), the tidewater glacier retreated rapidly by calving in the Adventdalen Valley in the early Holocene, around ca 11.3 kyr BP (ca 13 cal kyr BP), resulting in glaciomarine muddy deposits in our study area during the same period. A delta was formed at the end of the Adventdalen Valley around 9.2 kyr BP (ca. 10.3 cal kyr BP). According to Cable et al. (2018), plant macrofossils in deltaic deposits were dated between 7.8 and 5.6 cal kyr BP. This stage was not evident in our study area. Between 3.9 and 3.6 cal kyr BP, Oliva et al. (2014) reported peat accumulation within loess on terraces of the Adventdalen Valley. Later, at about 2.8 cal kyr BP, loess accumulation began on the terraces. According to Cable et al. (2018), the maximum age of loess accumulation increases up-valley. Traces of such peat and loess accumulation have not been found in our study area. Finally, the pingo dynamics in the Adventdalen Valley are described by Yoshikawa and Nakamura (1996), where the oldest date of about 7.8 cal kyr BP was from a pingo in the upper valley, from the middle valley was a pingo of about 2.8 cal kyr BP, and near the shore was a pingo dated by about 0.3 cal kyr BP. Middle Holocene ages of pingo sediments were also reported from our study area. In general, the Holocene landscape dynamics of the two areas, Adventdalen and Grøndalen, differ substantially.

Because the Arctic and its permafrost have warmed significantly and undergone considerable landscape transformations in recent times, understanding their evolution over geological timescales requires basic research to better understand the interactions between climate and permafrost. In this context, this study provides new data on permafrost's response to late-glacial and Holocene environmental changes on Svalbard.

6. Conclusions

Based on own and literature data, three main stages of landscape dynamics could be identified for the study region in the coastal areas of Isfjord and Grønfjord, comprising the Grøndalen and Hollendardalen valleys. The landscape evolution comprises the late-glacial deglaciation of the area (stage 1), the early Holocene marine transgression into the fjords (stage 2), and the middle- to late-Holocene terrestrial deposition and permafrost aggradation (stage 3). The last stage comprises substages of middle Holocene periglacial, fluvial, and alluvial deposition during the climate optimum (stage 3a), middle to late Holocene permafrost aggradation and pingo formation (stage 3b), and late Holocene slope and alluvial deposition, as well as pingo degradation (stage 3c).

Stage 1 of the deglaciation was inferred from the literature, based on radiocarbon-dated whale bones and marine shells. Marine diatom findings from a single exposure in the study area, and water extracts characterized by a dominant Na-Cl ion composition and high electrical conductivity, also supported the marine transgression stage 2.

The periglacial, fluvial, and alluvial deposition substage 3 is marked by alternate beddings of coarse-grained and fine-grained deposits and low ion content of water extracts. The pingo formation stage was inferred from the frequent occurrence of pingos in the Grøndalen Valley and low ionic content of pingo ice in the upper part, and higher ionic contents in the lower parts near the underlying sediments. The final stage of slope and alluvial deposition, and pingo degradation, is characterized by finer-grained deposits and thaw lakes on pingo tops.

Our research in West Spitsbergen indicates spatial and temporal changes in landscape dynamics and permafrost conditions driven by deglaciation, climate, and sea-level changes.

https://doi.org/10.5194/egusphere-2026-1377
Preprint. Discussion started: 12 June 2026

References

Antsiferova A.R., Siekkinen, E.D., and Chaus, O.M.: Аналитический обзор гидрометеорологических характеристик Западного Шпицбергена (по данным ГМО «Баренцбург») [Analytical review of the hydrometeorological characteristics of Western Svalbard (according to the GMO "Barentsburg")]. In: Savatyugin L.M. (ed.) Современное состояние природной среды архипелага Шпицберген: Коллективная монография [Current state of the natural environment of the Svalbard Archipelago: Collective monograph. St. Petersburg: Arctic Antarctic Research Institute. pp. 36–51 (in Russian), 2020.

Belousov K.N., Tsurikova N.M., Gradin B.E., and Shishlov S.B.: Роль рельефа в формировании современного облика природных ландшафтов архипелага Шпицберген (на примере о. Западный Шпицберген) [The role of the relief in the formation of the modern look of the natural landscapes of the Svalbard Archipelago (on the example of West Svalbard)]. In: Neizvestnov Ya.V., Semevskiy D.V. (eds.) Гидрогеология, инженерная геология, геоморфология архипелага Шпицберген [Hydrogeology, Engineering Geology, Geomorphology of the Svalbard Archipelago]. Leningrad: PGO Sevmorgeologiya. pp. 34–40 (in Russian), 1983.

Biskaborn B.K., Smith S.L., Noetzli J., Matthes H., Vieira G., Streletskiy D.A., Schoeneich P., Romanovsky V.E., Lewkowicz A.G. et al.: Permafrost is warming at a global scale. Nature Communications 10, 264. https://doi.org/10.1038/s41467-018-08240-4, 2019.

Blott S.J. and Pye K.: Gradistat: A grain size distribution and statistics package for the analysis of unconsolidated sediments. Earth Surface Processes and Landforms 26, 1237–1248. https://doi.org/10.1002/esp.261, 2001.

Brose D.: GEBAH – a software for the early detection of saltwater intrusions in freshwater-bearing aquifers and surface waters, independent of concentration. Brandenburgische Geowissenschaftliche Beiträge 24 (1/2), 69–82 (in German). Cottbus: Landesamt für Bergbau, Geologie und Rohstoffe. URL: https://lbgr.brandenburg.de/sixcms/media.php/9/BGB-1-2_17_Brose_69-82.pdf [last access: 11 March 2025], 2017.

Cable S., Elberling B., and Kroon A.: Holocene permafrost history and cryostratigraphy in the High-Arctic Adventdalen Valley, Central Svalbard. Boreas 47, 423–442. https://doi.org/10.1111/bor.12286, 2018.

Carter M.R. and Gregorich E.G. (eds.): Soil sampling and methods of analysis, 2nd edition. London: Taylor and Francis. 1264 pp. https://doi.org/10.1201/9781420005271, 2007.

Chernov R.A. and Muravyov A.Ya.: Современные изменения площади ледников западной части Земли Норденшельда (архипелаг Шпицберген) [Modern changes in the area of the glaciers of the western part and the Nordensköld Land (Svalbard archipelago)]. Лёд и Снег [Ice and Snow] 58(4), 462–472 (in Russian). https://doi.org/10.15356/2076-6734-2018-4-462-472, 2018.

Christiansen H.H., Etzelmüller B., Isaksen K., Juliussen H., Farbrot H., Humlum O., Johansson M., Ingeman-Nielsen T., Kristensen L. et al.: The Thermal State of Permafrost in the Nordic Area during the International Polar Year 2007–2009. Permafrost and Periglacial Processes 21, 156–181. https://doi.org/10.1002/ppp.687, 2010.

Christiansen H.H., Akerman J.H., and Repelewska-Pekalowa Y.: Active layer dynamics in Greenland. Svalbard and Sweden. In: Haeberli W., Brandova D. (eds.) Extended abstracts reporting current Research and new information. 8th International Permafrost Conference, 20-25 July 2003, Zurich, Switzerland. pp. 19–20. URL: https://www.permafrost.org/wp-content/uploads/ConferenceMaterials/08th-International-Conference-on-Permafrost-Proceedings-Zurich-Switzerland-20-25-July-2003.pdf. [last access: 11 March 2025], 2003.

Christiansen H.H., Gilbert G.L., Demidov N., Guglielmin M., Isaksen K., Osuch M., and Boike J.: Permafrost thermal snapshot and active-layer thickness in Svalbard 2016-2017. In: Orr. E., Hansen. G., Lappalainen. H., Hübner. C., Lihavainen H. (eds.) SESS Report 2018. The State of Environmental

https://doi.org/10.5194/egusphere-2026-1377
Preprint. Discussion started: 12 June 2026

Science in Svalbard – an annual report. Longyearbyen: SIOS. pp. 26–47. URL: www.sios-svalbard.org/sites/sios-svalbard.org/files/common/SESSreport_2018_FullReport.pdf. [last access: 11 March 2025]. 2019.

Christiansen H., Gilbert G., Neumann U., Demidov N., Guglielmin M., Isaksen K., Osuch M., and Boike J.: Ground ice content, drilling methods and equipment and permafrost dynamics in Svalbard 2016–2019 (PermaSval). In: Zaborska A, Methlie Hagen J.O., Moreno Ibáñez M., Lihavainen, H., Hübner C. (eds.) SESS report 2020 - The State of Environmental Science in Svalbard - an annual report. Longyearbyen: SIOS. 258–275 pp. https://doi.org/10.5281/zenodo.4294095, 2021.

Demidov N.E., Verkulich S.R., Karaevskaya E.S., Nikulina, A.L., and Savatyugin. L.M.: Первые результаты мерзлотных наблюдений на криосферном полигоне Российского научного центра на архипелаге Шпицберген (РНЦШ) [First results of permafrost observations at the monitoring site of the Russian Scientific Centre on Spitsbergen]. Проблемы Арктики и Антарктики [Problems of the Arctic and Antarctic] 1 (4), 67–79 (in Russian). URL: https://www.aaresearch.science/jour/article/view/82/80. [last access: 11 March 2025], 2016.

Demidov N., Wetterich S., Verkulich S., Ekaykin A., Meyer H., Anisimov M., Schirrmeister L., Demidov V., Hodson A.J.: Geochemical signatures of pingo ice and its origin in Grøndalen, West Spitsbergen. The Cryosphere 13, 3155–3169. https://doi.org/10.5194/tc-13-3155-2019, 2019.

Demidov N.E., Verkulich S.R., Demidov V.E., Soloveva D.A., and Wetterich S.: Permafrost in Spitsbergen and its monitoring at the Barentsburg cryosphere test site. In: Savatyugin L.M. (ed.) Современное состояние природной среды архипелага Шпицберген: Коллективная монография [Current state of the natural environment of the Svalbard Archipelago: Collective monograph. St. Petersburg: Arctic Antarctic Research Institute. pp. 135–149 (in Russian), 2020. a

Demidov N.E., Borisik A.L., Verkulich S.R., Wetterich S., Gunar A.Yu., Demidov V.E., Zheltenkova N.V., Koshurnikov A.V., Mikailova, V.M., Nikulina A.L., Novikov A.L., Savatyugin, L.M., Sirotkin A.N., Terekhov A.V., Ugryumov Yu.V., and Schirrmeister L.: Geocryological and hydrogeological conditions of Western part of Nordenskiold Land (Spitsbergen Archipelago). Izvestiya, Atmospheric and Oceanic Physics 56, 1376–1400. https://doi.org/10.1134/S000143382011002X, 2020. b

Demidov V., Wetterich S., Demidov N., Schirrmeister L., Verkulich S., Ekaykin A., Gagarin V., Koshurnikov A., Terekhov A., Veres A., and Kozachek A.: Pingo drilling reveals sodium-chloride dominated massive ice in Grøndalen, Spitsbergen. Permafrost and Periglacial Processes 32, 572–586. https://doi.org/10.1002/ppp.2124, 2021.

Demidov V., Demidov N., Verkulich S., and Wetterich S.: Distribution of pingos on Svalbard. Geomorphology 412, 108326. https://doi.org/10.1016/j.geomorph.2022.108326, 2022.

Demidov V., Verkulich S., Ekaykin A., Terekhov A., Veres A., Kozachek A., Wetterich S., Solovieva D., Varentsov M., and Barskov K.: Thaw slump development and other rapid permafrost disturbances in Hollendardalen Valley, Svalbard. Polar Science 42, 101122. https://doi.org/10.1016/j.polar.2024.101122, 2024.

Demidov V.E. and Terekhov A.V.: Distribution of Late Pleistocene ice-dammed lakes and ice-free oases on Svalbard. Relief and Quaternary deposits of the Arctic, Subarctic, and North-West Russia. Issue II. P. 87-94 (in Russian). https://doi.org/10.24412/2687-1092-2024-11-87-94.

Demidov N.E., Anisimov O.A., Anisimov M.A., et al. (2025). Conception and first results of the Russian National System of Background Permafrost Monitoring. Advances in Polar Science 36(1), 51-60 https://doi.org/10.12429/j.advps.2024.0036, 2024.

Denton G.H. and Hughes T.J. (eds.): The last great ice sheets. New York: Wiley Interscience, 484 pp.

Elvebakk A. (2005) A vegetation map of Svalbard on the scale 1:3.5mill. Phytocoenologia. Vol. 35. No. 4. P. 951–967. https://doi.org/10.1127/0340-269X/2005/0035-0951, 1981.

https://doi.org/10.5194/egusphere-2026-1377
Preprint. Discussion started: 12 June 2026

Farnsworth W.R., Allaart L., Ingólfsson Ó., Alexanderson H., Forwick M., Noormets R., Retelle M., and Schomacker A.: Holocene glacial history of Svalbard: Status. perspectives and challenges. Earth-Science Reviews 208, 103249. https://doi.org/10.1016/j.earscirev.2020.103249, 2020. a

Farnsworth W.R., Allaart L., Ingólfsson Ó., Alexanderson H., Forwick M., Noormets R., Retelle M., and Schomacker A.: The Svalhola Database. Dataset. PANGAEA. https://doi.org/10.1594/PANGAEA.921586, 2020. b

French H. and Shur Y.: The principles of cryostratigraphy. Earth-Science Reviews 101, 190–206. https://doi.org/10.1016/j.earscirev.2010.04.002, 2010.

Gentsch N., Mikutta R., Alves R.J.E., Barta J., Čapek P., Gittel A., Hugelius G., Kuhry P., Lashchinskiy N., Palmtag J. et al.: Storage and transformation of organic matter fractions in cryoturbated permafrost soils across the Siberian Arctic. Biogeosciences 12(14):4525-4542, https://doi.org/10.5194/bg-12-4525-2015, 2015.

Gilbert G.L., O'Neill H.B., Nemec W., Thiel C., Christiansen H.H., and Buylaert J.-P.: Late Quaternary sedimentation and permafrost development in a Svalbard fjord-valley, Norwegian High Arctic. Sedimentology 65, 2531–2558. https://doi.org/10.1111/sed.12476, 2018.

Hoefs J.: Stable Isotope Geochemistry. Berlin, Heidelberg: Springer, 201 pp., 1997.

Humlum O., Instanes A., and Sollid J.L.: Permafrost in Svalbard: a review of research history. climatic background and engineering challenges. Polar Research 22, 191–215. https://doi.org/10.3402/polar.v22i2.6455, 2003.

Koroleva N.E., Konstantinova N.A., Belkina O.A., Davydoc, D.A., Likhachev, A.Yu., Cavchenko, A.N., Yrbanavichenie, I.N.: Flora i rastitel'nost' poberezh'ya zaliva Gren-f'ord (arkhipelag Shpitsbergen) (Flora and vegetation of the Grenfjord area (Spitsbergen archipelago)). Apatity: K&M (Publ.). 132 p. (in Russ.), 2008.

Koroleva N.E.: Main types of plant communities In “Russian Spitzbergen”. Proceedings of the Karelian Research Center of the Russian Academy of Sciences 7. 3–23. https://doi.org/10.17076/bg323, 2016.

Krasilshchikov A.A.: Stratigraphy and paleotectonics of Precambrian-Early Paleozoic of Spitsbergen. Leningrad: Nedra. 120 pp. (in Russian), 1973.

Kriauchiunas V.V., Iglovski S.A., Lyubas A.A. et al. New paleogeography data of the eastern coast of Green Fjord (West Spitsbergen Island) based on research of the Holocene deposits on Finneset cape with use of isotope-geochemical methods. Izvestiya Tomskogo politekhnicheskogo universiteta. Inzhiniring resursov. Vol. 331. No 1. P. 171–183. (in Russ.). https://doi.org/10.18799/24131830-2020-1-2458, 2020.

Kusch S., Rethemeyer J., Ransby D., and Mollenhauer G.: Permafrost organic carbon turnover and export into a high-Arctic fjord: A case study from Svalbard using compound-specific 14C analysis. Journal of Geophysical Research: Biogeosciences 126, e2020JG006008. https://doi.org/10.1029/2020JG006008, 2021.

Landvik J.Y., Mangerud J., and Salvigsen O.: The Late Weichselian and Holocene shoreline displacement on the west-central coast of Svalbard. Polar Research 5(1), 29–44. https://doi.org/10.3402/polar.v5i1.6866, 1987.

Landvik J. Y., Mangerud J., and Salvigsen O.: Glacial history and permafrost in the Svalbard area. In: Senneset K. (ed.) Proceedings of the 5th International Conference on Permafrost. vol. 1. Trondheim: Tapir Publishers. pp. 194–198. URL: https://www.permafrost.org/wp-content/uploads/ConferenceMaterials/05th-International-Conference-on-Permafrost-1-Volume-Norway-1988.pdf. [last access: 12 March 2025], 1988.

Landvik J.Y., Bondevik S., Elverhøi A., Fjeldskaar W., Mangerud J., Salvigsen O., Siegert M.J., Svendsen J.I., and Vorren T.O.: The last glacial maximum of Svalbard and the Barents Sea area: ice sheet extent

https://doi.org/10.5194/egusphere-2026-1377
Preprint. Discussion started: 12 June 2026

and configuration. Quaternary Science Reviews 17, 43–75. https://doi.org/10.1016/S0277-3791(97)00066-8, 1998.

Lehmann H.W.: Geochemie und Genesis der Tiefenwässer der Nordostdeutschen Senke, Teil 1 [Geochemistry and genesis of the deep waters of the northeast German depression, part 1]. Zeitschrift für Angewandte Geologie, Berlin 20, 11, 502–509 (in German), 1974. a

Lehmann, H.W.: Geochemie und Genesis der Tiefenwässer der Nordostdeutschen Senke, Teil 2 [Geochemistry and genesis of the deep waters of the northeast German depression, part 2]. - Zeitschrift für Angewandte Geologie, Berlin 20, 12, S. 551-557 (in German), 1974. b

Liestøl, O.: Pingos, springs, and permafrost in Spitsbergen. Norsk Polarinstitutt Årbok 1975. Oslo: Norsk Polarinstitutt. pp. 7–29. URL: https://brage.npolar.no/npolar-xmlui/handle/11250/172803. [last access: 11 March 2025], 1977.

Livshits Yu.Ya.: Paleogene deposits and the platform structure of Spitsbergen. Leningrad: NIIGA, Nedra. 174. 160 pp. (in Russian), 1973.

Mangerud J., Bolstad M., Elgersma A., Helliksen D., Landvik J.Y., Lycke A.K., Lønne I., Salvigsen O., Sandahl T., and Sejrup H.P.: The Late Weichselian glacial maximum in western Svalbard. Polar Research 5(3), 275–278. https://doi.org/10.3402/polar.v5i3.6886, 1987.

Mangerud J. and Svendsen J.I.: Deglaciation chronology inferred from marine sediments in a proglacial lake basin. western Spitsbergen. Svalbard. Boreas 19 (3), 249–272. https://doi.org/10.1111/j.1502-3885.1990.tb00450.x. 1990.

Mangerud J., Bolstad M., Elgersma A., Helliksen D., Landvik J.Y., Lønne I., Lycke A.-K., Salvigsen O., Sandahl T., and Svendsen J.I. The last glacial maximum on Spitsbergen, Svalbard. Quaternary Research 38, 18–31. https://doi.org/10.1016/0033-5894(92)90027-G, 1992.

Mangerud J. and Svendsen J.I.: The Holocene Thermal Maximum around Svalbard. Arctic North Atlantic; molluscs show early and exceptional warmth. The Holocene 28(1), 65–83. https://doi.org/10.1177/0959683617715570, 2018.

Marshall C., Uguna J., Large D., Meredith W., Jochmann M., Friis B., Vane C., Spiro B., Snape C., and Orheim A.: Geochemistry and petrology of palaeocene coals from Spitzbergen — Part 2: Maturity variations and implications for local and regional burial models. International Journal of Coal Geology 143, 1–10. https://doi.org/10.1016/j.coal.2015.03.013, 2015.

Mavlyudov B.R., Savatyugin L.M., and Solovyanova I.Yu.: The reaction of the Nordenskjöld Glaciers (Svalbard) to climate change. Problems of the Arctic and Antarctic 1, 67–77 (in Russian), 2012.

Miller G.H., Sejrup H.P., Lehman S.J., and Forman S.L.: Glacial history and marine environmental change during the last interglacial-glacial cycle, western Spitsbergen, Svalbard, Boreas 18(3), 273-296, https://doi.org/10.1111/j.1502-3885.1989.tb00403.x, 1989.

Mollenhauer G., Grotheer H., Gentz T., Bonk E., and Hefter J.H.: Standard operation procedures and performance of the MICADAS radiocarbon laboratory at Alfred Wegener Institute (AWI). Germany. Nuclear Instruments and Methods in Physics Research Section B: Beam Interactions with Materials and Atoms 496, 45–51. https://doi.org/10.1016/j.nimb.2021.03.016, 2021.

Obidin N.I.: New data on groundwater and permafrost of the Soviet mines of Spitsbergen Island from 1952–1954 studies. Tr. NIIGA. 85(9). 129-140 (in Russian), 1958.

Oliva M., Vieira G., Pina P., Pereira P., Neves M., and Freitas M.C.: Sedimentological characteristics of ice-wedge polygon terrain in Adventdalen (Svalbard) – environmental and climatic implications for the late Holocene Solid Earth, 5, 901–914. https://doi.org/10.5194/se-5-901-2014, 2014.

Orheim A., Bieg Brekke T., Horseide V., and Stenvold J.: Petrography and geochemical affinities of Spitsbergen Paleocene coals. Norway. International Journal of Coal Geology 70, 116–136. https://doi.org/10.1016/j.coal.2006.04.008, 2007.

Piper A.: A graphic procedure in the geochemical interpretation of water-analyses. Transactions, American Geophysical Union 25(6), 914–928. https://doi.org/10.1029/TR025i006p00914, 1944.

https://doi.org/10.5194/egusphere-2026-1377
Preprint. Discussion started: 12 June 2026

Rechlin B.: Eine Methode zur konzentrationsunabhängigen Früherkennung von Salzwasserintrusionen in süßwasserführende Grundwasserleiter und Oberflächengewässer. [A method for concentration-independent early detection of saltwater intrusion into freshwater-bearing aquifers and surface waters]. Cottbus: Brandenburgische Geowissenschaftliche Beiträge, 15 (1/2), 57-68 (in German). URL: https://lbgr.brandenburg.de/sixcms/media.php/9/BGB-1-2_08_Rechlin_57-68.pdf. [last access: 12 March 2025], 2008.

Reimer P.J., Austin, W.E.N., Bayliss. A. et al.: The IntCal20 Northern Hemisphere radiocarbon age calibration curve (0–55 cal kBP). Radiocarbon 62(4), 725-757. https://doi.org/10.1017/RDC.2020.41, 2020.

Reineck H.-E. and Sing I.B.: Depositional Sedimentary Environments. 2nd edition. Berlin: Springer, 543 pp. https://doi.org/10.1007/978-3-642-81498-3,1980.

Salvigsen O.: Radiocarbon dated raised beaches in Kong Karls Land, Svalbard, and their consequences for the glacial history of the Barents Sea area. Geografiska Annaler 63A (3-4), 283–291. https://doi.org/10.1080/04353676.1981.11880043, 1981

Salvigsen O. and Nydal R.: The Weichselian glaciation in Svalbard before 15,000 B.P., Boreas 10(4), 433-446, https://doi.org/10.1111/j.1502-3885.1981.tb00507.x, 1981.

Schirrmeister L., Demidov N., Demidov V., Wetterich S., and Verkulich, S.R.: Sediment and ice characteristics of permafrost cores from Barentburg area, Westspitsbergen [dataset bundled publication]. PANGAEA, https://doi.org/10.1594/PANGAEA.963919, 2023.

Schirrmeister L., Grosse G., Wetterich S., Overduin Paul, Strauss J., Schuur E.A.G., and Hubberten H.-W.: Fossil organic matter characteristics in permafrost deposits of the Northeast Siberian Arctic. Journal of Geophysical Research 116, G00M02. https://doi.org/10.1029/2011JG001647, 2011.

Sharin V.V., Kokin O.V., Gusev E.A., Okunev A.S., Arslanov Kh.A., and Maksimov F.E.: New geochronological data from Quaternary sediments of the Nordenskiold Land area (the Spitsbergen Archipelago). Vestnik St. Petersburg State University. Ser. 7. Geology. Geography. Issue 1. 159–168 (in Russian), 2014.

Sirotkin A.N., Marine Yu.B., Kuznetsov N.B. et al.: The age of Spitsbergen basement consolidation: U–Pb dating of detrital zircons from the Upper Precambrian and Lower Carboniferous clastic rocks of the northwestern part of Nordenskjöld Land. Reports of RAS. 477(3). 1–6 (in Russian), 2017.

Snyder J.A., Miller G.H., Werner A., Jull A.J.T., and Stafford jr. T.W.: AMS-radiocarbon dating of organic-poor lake sediment. an example from Linnévatnet, Spitsbergen, Svalbard. The Holocene 4(4), 413–421. https://doi.org/10.1177/095968369400400409, 1994.

Snyder J.A., Werner A., and Miller G.H.: Holocene cirque glacier activity in western Spitsbergen. Svalbard: sediment records from proglacial Linnévatnet. The Holocene 10(5), 555–563. https://doi.org/10.1191/095968300667351697, 2000.

Soloveva D.A., Verkulich S.R., Pushina Z.V., Savelieva L.A., and Zazovskaya E.P.: Post-glacial changes in natural conditions in the northwestern part of Nordenskiöld Land (western Spitsbergen Island) based on the results of sediments studies in the Gröndalen Valley. Geomorfologiya i Paleogeografiya. Vol. 57. No.1. P. XX (in Russ.). https://doi.org/XX; https://elibrary.ru/XX(in press), 2026 (in Russian)

Svendsen J.I. and Mangerud. J.: Paleoclimatic inferences from glacial fluctuations on Svalbard during the last 20 000 years. Climate Dynamics 6, 213–220. https://doi.org/10.1007/BF00193533, 1992.

Svendsen J.I. and Mangerud J.: Holocene glacial and climatic variations on Spitsbergen, Svalbard. The Holocene 7, 45–57. https://doi.org/10.1177/095968369700700105, 1997.

Svendsen J.I., Elverhmi A., and Mangerud J.: The retreat of the Barents Sea Ice Sheet on the western Svalbard margin. Boreas 24, 244–256. https://doi.org/10.1111/j.1502-3885.1996.tb00640.x.

Valyashko, M.G. (1962) Geochemical rules of the potassium salt deposits formation. Moscow: Moscow University Publishing House. 402 pp. (in Russian), 1996.

https://doi.org/10.5194/egusphere-2026-1377
Preprint. Discussion started: 12 June 2026

Verkulich S., Zazovskaya E., Pushina Z., Savelieva L., Soloveva D., Demidov N., Shishkov V., and Dercon G.: The postglacial environmental changes in vicinity of the Barentsburg settlement (West Spitsbergen). Geophysical Research Abstracts 20, EGU2018-7729. URL: https://meetingorganizer.copernicus.org/EGU2018/EGU2018-7729.pdf. [last access: 11 March 2025], 2018.

Wenthworth C.K.: A scale of grade and class terms for clastic sediments. The Journal of Geology 30 (5), 377–392. https://doi.org/10.1086/622910, 1922.

Wetterich S., Rudaya N., Andreev A.A., Opel T., Schirrmeister L., Meyer H., and Tumskoy V.: Ice Complex formation in arctic East Siberia during the MIS3 Interstadial. Quaternary Science Reviews 84, 39-55. https://doi.org/10.1016/j.quascirev.2013.11.009, 2014.

Yoshikawa K. and Nakamura T.: Pingo growth ages in the delta area, Adventdalen, Spitsbergen. Polar Record 32 (183), 347–352. https://doi.org/10.1017/S0032247400067565, 1996.

https://doi.org/10.5194/egusphere-2026-1377
Preprint. Discussion started: 12 June 2026

Data availability: https://doi.org/10.1594/PANGAEA.963919

Author contribution: ND and VS carried out the numerous drillings and core descriptions and were responsible for parts of the laboratory analyses. DS was responsible for the paleoecological and geochronological results from the GD-1 outcrop. LS and SW organized the collaboration, sample preparation, and analysis at the Alfred Wegener Institute. SV was responsible for interpreting the data. LS, SW, and ND wrote the manuscript with contributions from all coauthors.

Competing interests: None of the authors has any competing interests.